The Astrophysical Journal, 905:58 (53pp), 2020 December 10 https://doi.org/10.3847/1538-4357/abb45c

The Zwicky Transient Facility Census of the Local Universe. I. Systematic Search for Calcium-rich Gap Transients Reveals Three Related Spectroscopic Subclasses

Kishalay De[1], Mansi M. Kasliwal[1], Anastasios Tzanidakis[1], U. Christoffer Fremling[1], Scott Adams[1], Robert Aloisi[2], Igor Andreoni[1], Ashot Bagdasaryan[1], Eric C. Bellm[3], Lars Bildsten[4,5], Christopher Cannella[1], David O. Cook[6], Alexandre Delacroix[7], Andrew Drake[1], Dmitry Duev[1], Alison Dugas[1,8], Sara Frederick[9], Avishay Gal-Yam[10], Daniel Goldstein[1], V. Zach Golkhou[3,11,21], Matthew J. Graham[1], David Hale[7], Matthew Hankins[1], George Helou[6], Anna Y. Q. Ho[1], Ido Irani[12], Jacob E. Jencson[13], David L. Kaplan[2], Stephen Kaye[7], S. R. Kulkarni[1], Thomas Kupfer[5], Russ R. Laher[6], Robin Leadbeater[14], Ragnhild Lunnan[15], Frank J. Masci[6], Adam A. Miller[16,17], James D. Neill[1], Eran O. Ofek[10], Daniel A. Perley[18], Abigail Polin[19,20], Thomas A. Prince[1], Eliot Quataert[19], Dan Reiley[7], Reed L. Riddle[7], Ben Rusholme[6], Yashvi Sharma[1], David L. Shupe[6], Jesper Sollerman[15], Leonardo Tartaglia[15], Richard Walters[7], Lin Yan[1], and Yuhan Yao[1]

[1] Cahill Center for Astrophysics, California Institute of Technology, 1200 E. California Blvd., Pasadena, CA 91125, USA; kde@astro.caltech.edu
[2] Center for Gravitation, Cosmology, and Astrophysics, Department of Physics, University of Wisconsin–Milwaukee, P.O. Box 413, Milwaukee, WI 53201, USA
[3] DIRAC Institute, Department of Astronomy, University of Washington, 3910 15th Ave. NE, Seattle, WA 98195, USA
[4] Department of Physics, University of California, Santa Barbara, CA 93106, USA
[5] Kavli Institute for Theoretical Physics, University of California, Santa Barbara, CA 93106, USA
[6] IPAC, California Institute of Technology, 1200 E. California Blvd., Pasadena, CA 91125, USA
[7] Caltech Optical Observatories, California Institute of Technology, Pasadena, CA 91125, USA
[8] Institute for Astronomy, University of Hawai'i, 2680 Woodlawn Dr., Honolulu, HI 96822, USA
[9] Department of Astronomy, University of Maryland, College Park, MD 20742, USA
[10] Benoziyo Center for Astrophysics, The Weizmann Institute of Science, Rehovot 76100, Israel
[11] The eScience Institute, University of Washington, Seattle, WA 98195, USA
[12] Department of Particle Physics and Astrophysics, Weizmann Institute of Science, Rehovot 7610001, Israel
[13] Steward Observatory, University of Arizona, 933 N. Cherry Ave., Tucson, AZ 85721-0065, USA
[14] Three Hills Observatory, The Birches CA71JF, UK
[15] Department of Astronomy, The Oskar Klein Centre, Stockholm University, AlbaNova, SE-10691 Stockholm, Sweden
[16] Center for Interdisciplinary Exploration and Research in Astrophysics (CIERA) and Department of Physics and Astronomy, Northwestern University, 2145 Sheridan Rd., Evanston, IL 60208, USA
[17] The Adler Planetarium, Chicago, IL 60605, USA
[18] Astrophysics Research Institute, Liverpool John Moores University, IC2, Liverpool Science Park, 146 Brownlow Hill, Liverpool L3 5RF, UK
[19] Department of Astronomy, University of California, Berkeley, CA, 94720-3411, USA
[20] Lawrence Berkeley National Laboratory, Berkeley, CA 94720, USA
Received 2020 April 19; revised 2020 August 7; accepted 2020 August 25; published 2020 December 11

Abstract

Using the Zwicky Transient Facility alert stream, we are conducting a large spectroscopic campaign to construct a complete, volume-limited sample of transients brighter than 20 mag, and coincident within 100″ of galaxies in the Census of the Local Universe catalog. We describe the experiment design and spectroscopic completeness from the first 16 months of operations, which have classified 754 supernovae. We present results from a systematic search for calcium-rich gap transients in the sample of 22 low-luminosity (peak absolute magnitude $M > -17$), hydrogen-poor events found in the experiment. We report the detection of eight new events, and constrain their volumetric rate to $\gtrsim$15% ± 5% of the SN Ia rate. Combining this sample with 10 previously known events, we find a likely continuum of spectroscopic properties ranging from events with SN Ia–like features (Ca-Ia objects) to those with SN Ib/c–like features (Ca-Ib/c objects) at peak light. Within the Ca-Ib/c events, we find two populations distinguished by their red ($g - r \approx 1.5$ mag) or green ($g - r \approx 0.5$ mag) colors at the r-band peak, wherein redder events show strong line blanketing features and slower light curves (similar to Ca-Ia objects), weaker He lines, and lower [Ca II]/[O I] in the nebular phase. We find that all together the spectroscopic continuum, volumetric rates, and striking old environments are consistent with the explosive burning of He shells on low-mass white dwarfs. We suggest that Ca-Ia and red Ca-Ib/c objects arise from the double detonation of He shells, while green Ca-Ib/c objects are consistent with low-efficiency burning scenarios like detonations in low-density shells or deflagrations.

Unified Astronomy Thesaurus concepts: Supernovae (1668); Compact objects (288); White dwarf stars (1799)

Supporting material: data behind figures, machine-readable tables

1. Introduction

Calcium-rich gap transients represent an emerging population of faint and fast-evolving supernovae (SNe) identified by their conspicuous [Ca II] emission in nebular-phase spectra (Perets et al. 2010; Sullivan et al. 2011; Kasliwal et al. 2012; Valenti et al. 2014; Lunnan et al. 2017; De et al. 2018a). Their photometric evolution is characterized by timescales and peak luminosities shorter and fainter than those of typical core-collapse and thermonuclear SNe, while their photospheric-phase

[21] Moore-Sloan, WRF Innovation in Data Science, and DIRAC Fellow.

velocities are largely similar to those of normal SNe Ib/c ($\sim$8000 km s^{-1}; see Filippenko 1997; Gal-Yam 2017 for a review). Yet, their most striking feature remains their preference for remote locations in the far outskirts of galaxies in old quiescent environments, in stark contrast to normal stripped-envelope SNe, which are found close to star formation (Perets et al. 2010; Lunnan et al. 2017). Together with the non-detection of any parent stellar populations in late-time imaging of the locations of these objects, their remote locations suggest that these transients arise from very old progenitors that may have traveled far away from their parent stellar population or were possibly formed in these remote locations (Yuan et al. 2013; Lyman et al. 2014, 2016; Perets 2014; Lunnan et al. 2017).

Their host offset distribution has been shown to be more skewed toward larger offsets than that of SNe Ia and even short gamma-ray bursts (Lunnan et al. 2017), while their hosts are preferentially found in group and cluster environments (Mulchaey et al. 2014; Foley 2015; Lunnan et al. 2017). Shen et al. (2019) show that the radial offset distribution of the sample may be consistent with that of globular clusters, and potentially indicative of a progenitor population that has been kicked out of nearby globular clusters.

The progenitors of Ca-rich gap transients remain unknown to date, and are currently only constrained with circumstantial evidence. Specifically, their remote locations and old host environments point to old progenitors involving white dwarfs (WDs) in binary systems. Suggested channels include helium shell detonations on WDs (Bildsten et al. 2007; Shen et al. 2010; Waldman et al. 2011; Sim et al. 2012; Dessart & Hillier 2015; Meng & Han 2015), double detonations of He shells on the surface of WDs (Sim et al. 2012; Polin et al. 2019a, 2019b), mergers of WDs with neutron stars (Metzger 2012; Margalit & Metzger 2016; Bobrick et al. 2017; Toonen et al. 2018; Zenati et al. 2019), tidal disruptions of WDs by intermediate-mass black holes (Rosswog et al. 2008; MacLeod et al. 2014; Sell et al. 2015; MacLeod et al. 2016; Sell et al. 2018; Kawana et al. 2020), and even extreme core-collapse SNe from highly stripped massive stars (Tauris et al. 2015; Moriya et al. 2017); however their old environments make core-collapse SNe unlikely (Perets et al. 2011). If they arise from binary WD systems, Meng & Han (2015) show that the old environments and consequently long delay times constrain the progenitor binary to consist of low-mass CO ($\lesssim$0.6 $M_{\odot}$) and He ($\lesssim$0.25 $M_{\odot}$) WDs.

Constraining their progenitors and rates is important not only for our understanding of these potentially common types of transients, but also for shedding light on a likely common end point in binary stellar evolution involving WDs in binary systems, and their possible significant contribution to the enrichment of the intergalactic medium with Ca (Mulchaey et al. 2014; Mernier et al. 2016). Estimates of the volumetric rates of this population from previous transient experiments include an estimate of 7% $\pm$ 5% of the SN Ia rate from the Lick Observatory Supernova Search (LOSS; Perets et al. 2010; Li et al. 2011) and a lower limit of $\approx$3% of the SN Ia rate from the Palomar Transient Factory (PTF; Kasliwal et al. 2012). A later estimate based on post-facto simulations of the detection efficiency and survey cadence of the PTF suggests that their rates may be as high as $\approx$30% of the SN Ia rate (Frohmaier et al. 2018). However, the sample of known objects was found largely by follow-up of isolated events outside of systematic SN classification efforts, leaving considerable uncertainty on the rates of the class.

The number of reported Ca-rich gap transients in the literature, as well as the diversity in their observed properties, has risen substantially in the last decade with large-scale optical transient surveys. As per the name of the class, the detection of strong [Ca II] emission in the nebular-phase spectra with a high [Ca II]/[O I] ratio[22] is the primary criterion used to relate objects to the class of Ca-rich transients (Valenti et al. 2014; Milisavljevic et al. 2017; De et al. 2018a). In addition, Kasliwal et al. (2012) defined this class of "gap" transients by their (i) faint peak luminosity, (ii) fast photometric evolution, (iii) photospheric-phase velocities similar to those of normal hydrogen-poor SNe ($\sim$8000 km s^{-1}), and (iv) early evolution to the nebular phase, notably without any constraints on the photospheric-phase spectra of the transient. These criteria are consistent with the prototype event of the class SN 2005E (Perets et al. 2010), which is also spectroscopically similar to SNe Ib near peak light.

There are seven other events in the class of Ca-rich gap transients that are spectroscopically similar to SNe Ib/c near peak light—SN 2007ke, SN 2010et, PTF 11bij (Kasliwal et al. 2012), SN 2012hn (Valenti et al. 2014), PTF 11kmb, PTF 12bho (Lunnan et al. 2017) and SN 2016hgs (De et al. 2018a). Other SNe Ic that show evidence of strong [Ca II] emission in the early nebular phase include iPTF 14gqr (De et al. 2018b), SN 2018kzr (McBrien et al. 2019) and SN 2019bkc (Chen et al. 2020; Prentice et al. 2020), although they are more luminous ($M_{\rm peak} \lesssim -17.5$) than the typical Ca-rich gap transient. However, spectroscopic similarity to SNe Ib/c does not appear to be a defining characteristic of the class. Notable exceptions include PTF 09dav (Sullivan et al. 2011; Kasliwal et al. 2012) and SN 2016hnk (Galbany et al. 2019; Jacobson-Galán et al. 2020), which exhibit similarities to subluminous SN 1991bg–like SNe Ia (Filippenko et al. 1992) near peak light.

Similarly, iPTF 15eqv (Milisavljevic et al. 2017) is a peculiar hydrogen-rich SN IIb that exhibits a high [Ca II]/[O I] ratio in nebular-phase spectra, which show that it is luminous at peak and consistent with a core-collapse SN in a star-forming environment. Another potential member of the class, SN 2005cz (Kawabata et al. 2010; Perets et al. 2011), exhibits a high [Ca II]/[O I] ratio in its nebular-phase spectrum; yet the lack of photometry around peak light precludes a confirmed association with this class of faint and fast-evolving transients, as is the case for several candidates presented in Filippenko et al. (2003).

The large heterogeneity in the peak luminosity and spectroscopic appearance of objects likely points to a diversity in explosions that produce high [Ca II]/[O I] in their nebular-phase spectra. Yet, the small number of total reported events ($\lesssim$10) has prevented a holistic analysis of the spectroscopic and photometric properties of this class. Most previous studies have focused on one or two events, each of which has been suggested to be a unique member of this emerging population which remains poorly understood. In particular, previous works have not characterized the nebular-phase behavior of a systematically selected sample of low-luminosity hydrogen-poor transients to be able to quantitatively place the photometric and spectroscopic properties of the class of Ca-rich gap

[22] Throughout this paper, we refer to the flux ratio of the forbidden [Ca II] $\lambda\lambda$7291, 7324 to [O I] λ6300, 6364 lines as [Ca II]/[O I].

transients in a broader context. Such an analysis with a large sample can yield vital clues to trends within the population and shed light on the underlying explosions. The aim of this paper is to systematically uncover and analyze this population of faint and fast-evolving hydrogen-poor events that exhibit high [Ca II]/[O I] in nebular-phase spectra.

While galaxy-targeted SN surveys are sensitive to transients occurring close to their host galaxies, the known preference of these transients for large host offsets necessitates a wide-field search approach that is sensitive to transients at large projected offsets from their host galaxies. Given the faint peak luminosity ($M_r \approx -16$) and relatively low volumetric rates ($\sim$10% of SN Ia rate) of these events, finding a large sample of events requires a sufficiently deep (depth $r \gtrsim 20$ mag to find events out to $\approx$150 Mpc) optical all-sky survey with a cadence of $\lesssim$4 days to detect these short-lived events. At the same time, due to the high rate of higher-redshift SNe Ia at this depth ($\sim$8500 yr^{-1} down to $r = 20$ mag limiting magnitude; Feindt et al. 2019), finding a systematic sample of these local universe events requires a targeted approach to classify transients in the local universe by cross-matching transients to known nearby galaxies. Such an approach is now possible with large catalogs of galaxies with known spectroscopic redshifts like the Census of the Local Universe (CLU; Cook et al. 2019) catalog and GLADE (Dálya et al. 2018).

This paper presents the first in a series of publications from the CLU experiment of the Zwicky Transient Facility (ZTF; Bellm et al. 2019a; Graham et al. 2019). This paper provides an overview of the sample selection and spectroscopic completeness of this volume-limited experiment. Here, we focus on the identification of Ca-rich gap transients, specifically on the class of faint and hydrogen-poor transients that exhibit Ca-rich spectra in the nebular phase. We briefly describe the design of the experiment and sample selection in Section 2. Section 3 presents an analysis of the photometric and spectroscopic properties of the combined sample of transients from ZTF and the literature, specifically noting the presence of two spectroscopic classes and a continuum of properties across these classes. Using the controlled selection criteria of the experiment, we present an analysis of the host environments of these transients in Section 4 while Section 5 presents a discussion on the estimated volumetric rates of these events. In Section 6, we combine all of the results to constrain the progenitors of this class and we summarize our conclusions in Section 7.

Calculations in this paper assume a WMAP9 flat ΛCDM cosmology with $H_0 = 69.3$ km s^{-1} Mpc^{-1} and $\Omega_M = 0.286$ (Hinshaw et al. 2013). We use the median redshift-independent distance estimates from the NASA Extragalactic Database (NED) for transients hosted in galaxies that have such measurements, and redshift-derived distance estimates otherwise. For the redshift-derived distance estimates in this local universe sample ($z < 0.05$), the typical uncertainty in the luminosity distance and projected offsets is $\lesssim$5% for peculiar velocities $\lesssim 300$ km s^{-1}. Times reported are in Universal Time throughout this paper.

2. Observations

2.1. The CLU Experiment

The ZTF is a wide-field optical time-domain survey running out of the 48 inch Schmidt telescope (P48) at Palomar Observatory (Bellm et al. 2019a; Graham et al. 2019). With a field of view of 47 square degrees, the instrument achieves a median limiting magnitude of $r \approx 20.5$ mag in 30 s exposures of the sky and a survey speed of $\approx$3750 square degrees per hour (Dekany et al. 2016). The ZTF observing time is divided into a public component (40%), a collaboration component (40%), and a Caltech component (20%). Bellm et al. (2019b) provide an overview of the various ZTF surveys undertaken in the first year of operations, and the survey scheduling system designed to carry out operations to maximize volumetric survey speed.

The public component is a 3 day cadence $g + r$ survey of the entire northern sky ($\approx$34% of P48 time) together with a 1 day cadence $g + r$ survey of the Galactic plane ($\approx$6% of P48 time). The collaboration time is dedicated to high-cadence ($3g + 3r$ per night) observations of $\approx$2500 square degrees and a slower-cadence ($\approx$4 days) i-band survey. The Caltech time is dedicated to a one-night cadence $g + r$ survey of $\approx$3000 square degrees. Transients in the difference imaging pipeline (based on the ZOGY subtraction algorithm; Zackay et al. 2016) of ZTF (Masci et al. 2019) are reported and distributed in Avro alert packets[23] (Patterson et al. 2019), including photometry and metadata for the detected transient, as well as a 30 day history for previous detections and non-detections.

The ZTF CLU experiment has been designed to build up a spectroscopically classified sample of transients in the local universe (within 200 Mpc) by classifying all transients found coincident with galaxies in the CLU (Cook et al. 2019) catalog. The CLU catalog consists of $\sim$234,500 galaxies with previously known redshifts compiled from several previous spectroscopic surveys (called CLU-compiled; see Cook et al. 2019), along with additional nearby galaxies found in a wide, narrowband (Hα) survey covering 3π of the northern sky with the Palomar 48 inch telescope (Cook et al. 2019).

The initial filter for the experiment used the CLU-compiled catalog together with $\sim$1000 of the highest-significance ($>25\sigma$) candidates from the Hα survey. Starting from 2019 April, we initiated the use of the next data release, which included a larger sample ($\approx$38,000 candidates with significance $>3\sigma$) of high-confidence nearby galaxies from the CLU Hα survey (see Cook et al. 2019 for a description). Based on the transient sample found in this experiment, we found that $\approx$1% of the transients were hosted in the CLU Hα survey galaxies before the 2019 April update, while $\approx$10% of the transients were hosted in galaxies from the Hα catalog following the inclusion of the next data release.

The CLU experiment was initiated on 2018 June 1 and we restrict the sample of transients in this paper to events saved until 2019 September 30. The sample selection for the transients was implemented as a part of a custom filter implemented on the Global Relay of Observatories Watching Transient Happen (GROWTH) Marshal (Kasliwal et al. 2019), which is a web portal for vetting and coordinating follow-up of transients. The selection criteria for ZTF alerts to be saved in the CLU experiment were as follows:

1. Each alert packet was spatially cross-matched to the CLU catalog of galaxies. The size of the spatial cross-match was set to $3 \times D_{25}$, where D_{25} is the isophotal major axis containing 25% of the total light of the galaxy, as contained in the CLU catalog. If a D_{25} radius was not

[23] https://avro.apache.org

available for the galaxy, a default cross-match radius of 280″ was used.[24] The cross-matching was performed on the dedicated time-domain astronomy server called `kowalski` at Caltech (Duev et al. 2019).
2. The alert candidate was produced as a positive candidate in the subtraction, i.e., the source flux increased from the reference image.
3. The alert candidate had a real–bogus score of >0.3 as classified by the ZTF machine-learning algorithm (Mahabal et al. 2019). This choice produced a false negative rate of <3% (Duev et al. 2019).
4. The alert candidate was at least 20″ away from a star brighter than 15.0 mag.
5. Alert candidates within 1″ of a known star in Pan-STARRS1 (PS1; Chambers et al. 2016) were rejected. The identification of stars was based on the machine learning–based star/galaxy classification score presented in Tachibana & Miller (2018), which was available for the three nearest sources in the ZTF alert packets. We used an `sgscore` threshold of 0.6, i.e., candidates within 1″ of a PS1 source with an `sgscore` > 0.6 were rejected.
6. The alert candidate was at least 2″ away from the nearest solar system object and was detected at least twice in the survey separated by 50 minutes. The former criterion removed known asteroids in the ZTF alert stream while the latter removed unknown solar system objects.

No further magnitude cut was applied to this transient stream. This filter produced typically ≈100 sources to be vetted by on-duty astronomers every day, which involved an inspection of the science, reference and difference image cutouts contained in the ZTF alert packets. Human vetting was required to remove alerts from remaining stellar sources that passed the filter, remove variability from known active galactic nuclei (AGNs), and identify remaining bogus sources before assigning appropriate spectroscopic follow-up. For 2018 and 2019, spectroscopic follow-up was exclusively limited to transients within 100″ of the nearest CLU galaxy to remove the large amount of contamination of SNe in background galaxies. In addition, transients coincident with known background galaxies (with known spectroscopic redshifts or photo-$z > 0.1$) were excluded from the sample in order to avoid a large number of false positives from background AGNs and SNe Ia.

As such, the experiment may have been incomplete, excluding transients occurring at very large projected offsets of >100″ from their parent galaxies, corresponding to a physical projected distance of 100 kpc at 200 Mpc, 50 kpc at 100 Mpc, and 25 kpc at 50 Mpc. In addition, sources coincident with known AGNs and having a long-term history of variability were not assigned for follow-up. On average, 10–15 SNe were saved for spectroscopic follow-up every week, which were coordinated via source pages on the GROWTH Marshal. Starting from 2019 November, sources from the public ZTF data stream were reported to the Transient Name Server (TNS[25]) as soon as they were saved by a human scanner (De et al. 2019a).

All transients saved after this vetting process were systematically assigned for spectroscopic follow-up. We prioritized follow-up of sources that were brighter than or were going to peak at brighter than 20 mag (in either $r_{\rm ZTF}$ or $g_{\rm ZTF}$; see Bellm et al. 2019a), which was selected to be the target limiting magnitude for the experiment. Given the typical ZTF limiting magnitude of 20.5 mag, we did not apply any magnitude cuts to the filter to be able to track the photometric evolution and assign follow-up for transients peaking around 20 mag. Spectroscopic classifications were performed using a multi-tiered approach—(i) sources brighter than 19 mag were assigned for spectroscopic follow-up on the robotic Spectral Energy Distribution Machine (SEDM; Blagorodnova et al. 2018), (ii) sources between 19 and 20 mag were assigned for spectroscopic follow-up on the Double Beam Spectrograph (DBSP; Oke & Gunn 1982) on the 200 inch Hale telescope (P200) at Palomar Observatory, and (iii) sources fainter than 20 mag were assigned for lower-priority follow-up on P200 + DBSP.

Sources assigned to the SEDM queue remained as follow-up targets for a duration of 7 days, after which they were re-assigned to SEDM if still brighter than 19 mag or to P200 otherwise. Spectroscopic follow-up on P200 was required for bright sources (<19 mag) coincident with the nuclei of nearby galaxies, where host galaxy contamination was difficult to remove in the SEDM spectra. In cases where P200 classifications were not possible due to poor weather or due to large host contamination in P200 data for faint targets, we also used the Low Resolution Imaging Spectrometer (LRIS; Oke et al. 1995) on the Keck I telescope for spectroscopic classifications.

The spectroscopic follow-up effort for bright sources ($m < 19$ mag) was coordinated with the Bright Transient Survey (BTS; Fremling et al. 2019) experiment, which aims to classify all transients brighter than 19 mag in the ZTF public alert stream. Community follow-up for bright transients overlapping with BTS also aided in the spectroscopic classification completeness of the sample. Classifications were done with the `SuperNova IDentification` (SNID; Blondin & Tonry 2007) code by automatic execution on spectra produced by the SEDM automated pipeline (Rigault et al. 2019) and by manual execution for all other instruments. For spectra contaminated by the underlying host light, we used `superfit` (Howell et al. 2005) to attempt host subtraction and derive a classification. The final classification was made by human inspection of the best-fit templates matched from SNID or `superfit`.

2.2. Spectroscopic Completeness

The aim of the tiered approach to spectroscopic classification was to obtain high spectroscopic completeness for transients that peaked brighter than 20 mag in galaxies within the local universe. This magnitude limit corresponds to a luminosity completeness of $M < -16.5$ mag for all galaxies in the 200 Mpc volume of the CLU catalog and $M < -15$ mag for galaxies within 100 Mpc. However, given the galaxy-targeted nature of the target selection, the experiment was not sensitive to transients that occurred in nearby galaxies with previously unknown spectroscopic redshifts. Based on results from the ZTF BTS, the completeness (in terms of galaxy count) of the compiled catalog was ≈80% at the lowest redshifts and decreased to ≈50% at the edge of the 200 Mpc volume (Fremling et al. 2019).

While an effort was made to have complete spectroscopic classifications to a depth of ≈20 mag, classifications were not always possible due to several reasons. These included the

[24] 280″ is 3× the median D_{25} value of all galaxies in the CLU catalog.
[25] https://wis-tns.weizmann.ac.il/

difficulty of following up transients found close to the Sun and of classifying transients on the nuclei of bright galaxies (where low-resolution SEDM spectra were dominated by host galaxy light) that faded before a scheduled run on the P200/Keck, and the loss of P200/Keck time in periods of bad weather. We thus evaluated the spectroscopic completeness of the experiment in the first year of operations.

We restricted this sample to transients that were saved between[26] 2018 June 1 and 2019 September 30, and to sources detected in any of the public or internal collaboration surveys (note that the public survey has the largest footprint on the sky). We defined our primary sample of sources such that they were detected at least twice, and peaked at a magnitude brighter than 20 mag in either the $r_{\rm ZTF}$ or the $g_{\rm ZTF}$ filter. We required at least two detections of the transient separated by 50 minutes during the survey, as implemented in the alert filter. Multiple detections in the same filter on a single night were averaged to estimate the transient flux on each night.

A total of 852 candidate SNe were saved during this time period, out of which 563 were also included in the BTS program. Of these 852 events, 754 were reliably classified, while 98 were unclassified either due to the lack of follow-up spectroscopy or due to ambiguous classifications from spectroscopic data. As such, the spectroscopic completeness of the complete acquired sample was 88.5% for all transients that had at least one detection brighter than 20 mag. The corresponding classification completeness for $m_{\rm peak} < 19$ mag was 92.9%, that for $m_{\rm peak} < 18$ mag was 98.0%, and that for $m_{\rm peak} < 17$ mag was 98.6% for the entire experiment duration mentioned above. We show a cumulative plot of the number of sources saved and classified as a function of the peak magnitude in Figure 1.

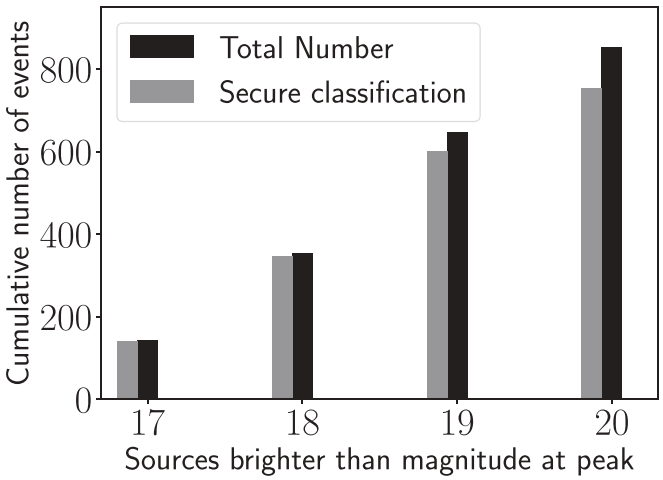

Figure 1. Cumulative number of events that were saved (in black) and classified (in gray) as a function of the peak magnitude in the CLU sample of events.

2.3. Sample of Ca-rich Gap Transients

This work focuses on the sample of Ca-rich gap transients identified in this experiment in the aforementioned period of operations (i.e., from 2018 June 1 to 2019 September 30). Given the large number of SNe that were classified as a part of the experiment, it was not possible to perform a nebular-phase spectroscopic follow-up of all events. We thus identified candidate Ca-rich gap transients with simple selection criteria using photometry from the ZTF survey and peak light spectroscopic properties (from the classification effort), focusing on the population of hydrogen-poor low-luminosity events in the sample. Although the criteria were motivated by the known properties of the previous sample of events, we deliberately kept these minimal for candidate selection due to the uncertainties on the intrinsic properties of the class and the small number of previously reported events. The candidate selection criteria were as follows:

1. The transient should have a peak luminosity (in the $g_{\rm ZTF}$ or $r_{\rm ZTF}$ filter) fainter than $M = -17$ mag at the known redshift of the host galaxy (after correcting for Galactic extinction, but not for possible host galaxy extinction). We required at least two detections on the rise of the light curve in the same filter to be able to constrain the peak luminosity.
2. The spectroscopic properties of the source should be consistent with a hydrogen-poor SN near peak light. We did not include any events that exhibited broad hydrogen features in their spectra (i.e., Balmer lines that did not emanate from the underlying host galaxy). We obtained at least one epoch of late-time (at $\gtrsim$30 days after peak light) spectroscopy with DBSP and LRIS on the Keck I telescope for events that passed (1) and this criterion.
3. We required that the sources exhibit an early transition to the nebular phase, which we confirmed by either the appearance of nebular emission lines and a fading continuum starting at +30 days from peak light or a complete transition to the nebular phase by $\approx$150 days after peak light.
4. As strong [Ca II] emission is the hallmark feature of this class, we required that the nebular-phase spectrum exhibit [Ca II]/[O I] > 2 (Milisavljevic et al. 2017; De et al. 2018a) at any phase where the spectrum exhibited nebular emission lines.

Comparing the selection criteria to those of Kasliwal et al. (2012), we note that we did not select candidates based on the fast photometric evolution or photospheric-phase velocities. This choice made us more sensitive to events with larger diversity in ejecta masses and velocities. After applying selection criteria (1) and (2) to the sample of events in the volume-limited experiment, we were left with 22 events, which were followed up with spectroscopy in the nebular phase. Seven of these 22 sources were found to qualify for the criterion [Ca II]/[O I] > 2 in the nebular phase, which defined the primary sample for this paper. In addition, we present observations of SN 2018gwo, a nearby SN Ic that was not detected in ZTF data before its peak (due to a maintenance break in 2018 October), but was recovered on its radioactive decline tail. Combining these observations with publicly available photometry and spectroscopy, we show that SN 2018gwo is a likely Ca-rich gap transient at a distance of 28 Mpc.

We applied the same selection criteria to the published literature sample of Ca-rich gap transients to include them as our comparison sample. The set of 10 literature events satisfying our cuts comprised SN 2005E, SN 2007ke, PTF 09dav, SN 2010et, PTF 11bij, SN 2012hn, PTF 11kmb, PTF 12bho, SN 2016hgs,

[26] Accounting for observation gaps due to instrument maintenance and poor weather, this period covered a total of 390 nights of full or partial ZTF operations.

Table 1
Summary of the Properties of the Faint Hydrogen-poor Transients Selected for Nebular Phase Follow-up in This Work

Object	R.A. J2000	Decl. J2000	Spec. Type	Peak r Mag. (Abs. Mag.)	[Ca II]/[O I] Flux Value/Phase (days)	Redshift	Host Offset ($''$/kpc)
ZTF 18aayhylv/SN 2018ckd	$14^h06^m11^s.94$	+09°20′39.″33	Ca-Ib	−16.17	>3.38/+58	0.024	39.03/19.08
ZTF 18abmxelh/SN 2018lqo	$16^h28^m43^s.26$	+41°07′58.″66	Ca-Ib	−16.21	>12.5/+49	0.033	23.25/15.46
ZTF 18abttsrb/SN 2018lqu	$15^h54^m11^s.47$	+13°30′50.″87	Ca-Ib	−16.44	>8.38/+31	0.036	37.12/26.70
ZTF 18acbwazl/SN 2018gwo*	$12^h08^m38^s.82$	+68°46′44.″42	Ca-Ic	< −16.0	5.16/+53	0.008	54.20/8.56
ZTF 18acsodbf/SN 2018kjy	$06^h47^m17^s.96$	+74°14′05.″90	Ca-Ib	−15.63	4.44/+111	0.018	17.18/6.35
ZTF 19aaznwze/SN 2019hty	$12^h55^m33^s.03$	+32°12′21.″70	Ca-Ib	−16.38	>3.27/+38	0.023	18.74/8.73
ZTF 19abrdxbh/SN 2019ofm	$14^h50^m54^s.65$	+27°34′57.″59	Ca-Ia	−17.03	>2.13/+175	0.030	18.24/11.16
ZTF 19abwtqsk/SN 2019pxu	$05^h10^m12^s.60$	-00°46′38.″63	Ca-Ib	−16.56	>8.30/+146	0.028	30.93/17.56
ZTF 19aamfupk/SN 2019ccm	$04^h41^m05^s.36$	+73°40′23.″10	SN Ib	−16.40	1.18/+207	0.015	14.73/4.54
ZTF 19aanfsmc/SN 2019txl	$09^h32^m59^s.36$	+27°30′07.″80	SN Ib	−16.21	0.87/+330	0.034	11.68/7.96
ZTF 19aasqseq/SN 2019txt	$09^h59^m06^s.38$	+17°49′09.″99	SN Ib	−15.90	1.34/+180	0.026	19.94/10.69
ZTF 19abgqruu/SN 2019mjo	$00^h06^m59^s.83$	+03°27′39.″70	SN Ib-pec	−16.62	NN/+180	0.041	12.38/10.06
ZTF 18abdffeo/SN 2018dbg	$14^h17^m58^s.86$	+26°24′44.″59	SN Ib/c	−16.65	NN/+22	0.015	2.01/0.61
ZTF 19aarrdoz/SN 2019txr	$08^h42^m31^s.91$	+56°17′42.″19	SN Ib/c	−16.73	<1/+270	0.044	1.95/1.71
ZTF 18aboabxv/SN 2018fob	$15^h13^m07^s.23$	+41°16′11.″07	SN Ic	−16.93	0.87/+212	0.029	18.47/10.84
ZTF 19aadttht/SN 2019yz	$15^h41^m57^s.30$	+00°42′39.″41	SN Ic	−16.63	0.59/+242	0.006	34.17/4.54
ZTF 19aadwtoe/SN 2019abb	$07^h54^m17^s.26$	+14°16′22.″42	SN Ic	−16.56	0.79/+357	0.015	4.26/1.34
ZTF 19aailcgs/SN 2019ape	$10^h51^m42^s.55$	+18°28′52.″62	SN Ic	−16.62	0.87/+180	0.021	11.53/4.79
ZTF 19abhhdwf/SN 2019ouq	$17^h01^m41^s.94$	+30°06′34.″43	SN Ic	−16.68	<1/+170	0.036	8.71/6.27
ZTF 18acushie/SN 2018kqr	$08^h50^m03^s.60$	+55°10′09.″54	SN Ic-BL	−16.75	NN/+16	0.045	3.15/2.82
ZTF 19aavlfvn/SN 2019gau	$14^h38^m10^s.42$	+10°08′04.″93	SN Ia	−16.75	—/ +260	0.028	1.30/0.73
ZTF 19aawhlcn/SN 2019gsc	$14^h37^m45^s.25$	+52°43′36.″28	SN Ia 02cx	−13.90	NN/+60	0.011	10.99/2.50
ZTF 19abalbim/SN 2019ttf	$18^h42^m15^s.87$	+24°53′48.″99	SN Ia 02cx	−13.99	NN/+230	0.011	11.07/2.52

Note. The column Spec. Type only refers to the spectroscopic appearance of the object near peak light. The Ca-rich objects are indicated with Ca in the Spec. Type column. For cases where the object did not turn nebular even at the latest phases of spectroscopic follow-up, we indicate the [Ca II]/[O I] flux ratio with NN and indicate the phase of the latest available spectrum. In the case of SN 2018gwo (indicated with *), the object did not pass the primary selection criteria but is a likely Ca-rich gap transient when we combined publicly available photometry and nebular-phase follow-up from our campaign. Details on the objects that did not pass the nebular-phase criterion are discussed in Appendix, highlighting why each object was excluded from the Ca-rich sample. For one event (SN 2019gau), we did not detect nebular emission features and hence denote the [Ca II]/[O I] ratio with –.

and SN 2016hnk. Table 1 summarizes the photometric and spectroscopic properties of all the transients identified for nebular phase follow-up. Here, we describe the initial detection to the final classification of each of the individual objects in the sample of Ca-rich gap transients presented in this paper. We present a discussion of the properties of the remaining objects that passed the light-curve criteria but did not pass the nebular-phase criterion in Appendix, specifically highlighting how we determined the Ca-rich classification for each event. Henceforth, we refer to all phases with respect to the time of the r-band peak (see Section 3.3.1).

2.3.1. SN 2018ckd/ZTF 18aayhylv

ZTF 18aayhylv (=SN 2018ckd) was first detected in the ZTF difference imaging pipeline on 2018 June 7.19 (Modified Julian Date (MJD) = 58,276.19) at J2000 coordinates α = 14:06:11.95 and δ = 09:20:39.3, at a magnitude of $r = 19.39 \pm 0.09$ mag. The transient passed the filter on the GROWTH Marshal on 2019 June 10 (second detection) and was saved for spectroscopic follow-up. The transient was detected by the Catalina Real-time Transient Survey (Drake et al. 2009) on 2019 June 12, was reported to the TNS on the same date (Crts 2018), and was assigned the International Astronomical Union (IAU) name AT 2018ckd. The transient was not detected in the ZTF alert production pipeline on 2018 June 1.31 to a 5σ limit of $r \approx 19.82$ mag. However, the transient was detected at $\approx 4\sigma$ significance with $r \approx 20.25$ mag with forced photometry (see Section 2.4) at the transient location in the ZTF difference images (Masci et al. 2019). The last non-detection of the source in forced photometry was at 2018 May 29.31 down to a 5σ limit of $r \approx 19.65$ mag.

The transient was found in the outskirts of NGC 5463, an S0 galaxy at $z = 0.024$ (Figure 2), at a projected offset of $\approx 39.''0$ from the host center, corresponding to a physical separation of $\approx$19.1 kpc. We obtained a spectrum of ZTF 18aayhylv with DBSP on 2018 June 12, which exhibited P-Cygni features of He I and Ca II similar to SNe Ib. Subsequent photometry from ZTF and follow-up with P60 + SEDM confirmed a faint and fast-evolving (rise time $\lesssim$ 15 days) light curve peaking at an absolute magnitude of $M \approx -16.0$ mag (Figure 3). A nebular-phase spectrum of the source at $\approx$+60 days from the r-band peak with LRIS on the Keck I telescope showed strong [Ca II] emission lines with weak [O I] emission, confirming an early transition to the nebular phase and the classification of this source as a Ca-rich gap transient.

2.3.2. SN 2018lqo/ZTF 18abmxelh

ZTF 18abmxelh (=SN 2018lqo) was first detected in the ZTF difference imaging pipeline on 2018 August 10.18 (MJD = 58,340.18) at J2000 coordinates α = 16:28:43.26 and δ = 41:07:58.7, at a magnitude of $r = 20.11 \pm 0.17$ mag. The transient passed the machine-learning thresholds on the GROWTH Marshal on 2019 August 16 and was saved for spectroscopic follow-up. We reported the transient to the TNS on 2019 October 28 (De 2019a), leading to its IAU name of AT 2018lqo. With forced photometry on the ZTF difference

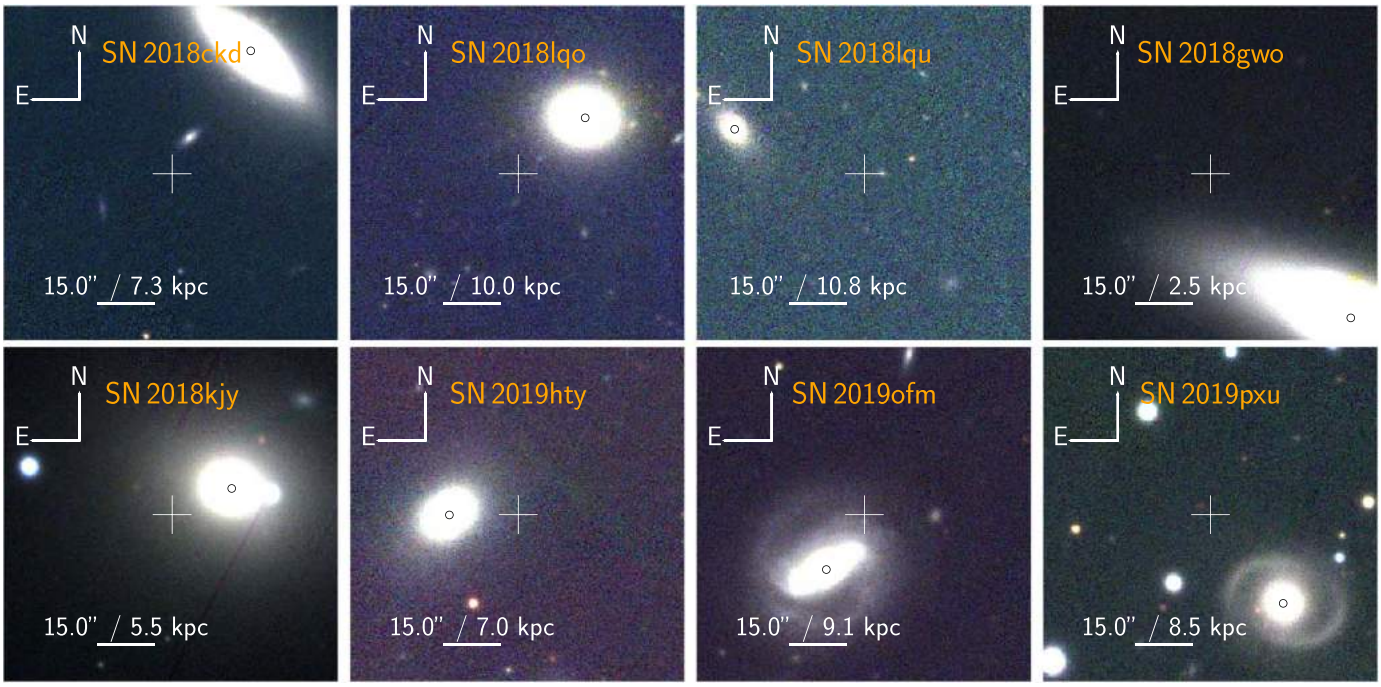

Figure 2. RGB composite archival images of the locations of the eight Ca-rich gap transients in the ZTF CLU sample. The images were taken from the PS1 survey (Chambers et al. 2016). In each panel, the white cross-hair shows the location of the detected transient and the scale shows the projected angular size and physical scale at the redshift of the host galaxy. The apparent host galaxy is marked with a black circle at its core in each panel.

images, we found that the transient was not detected on 2018 August 07.18 (MJD = 58,337.18) down to a 5σ limit of $r \approx 21.16$ mag. The transient exhibited an initial fading of $\approx$0.7 mag in $\approx$3 days following the first detection, followed by a rise to a peak $\approx$10 days later.

The transient was found in the outskirts of CGCG 224-043, an E-type galaxy at $z = 0.032$ (Figure 2), at a projected offset of $\approx 23\farcs2$, corresponding to a physical separation of $\approx$15.5 kpc. We obtained a spectrum of ZTF 18abmxelh with DBSP on 2018 August 21, which exhibited P-Cygni features of He I and Ca II similar to SNe Ib. Subsequent photometry from ZTF and follow-up with P60 + SEDM indicated a faint and fast-evolving (rise time $\lesssim$ 15 days) light curve peaking at an absolute magnitude of $M \approx -16.1$ mag (Figure 3). A nebular-phase spectrum of the source at $\approx$+50 days from the r-band peak with LRIS on the Keck I telescope showed strong [Ca II] emission lines, confirming a fast nebular-phase transition and the classification of this source as a Ca-rich gap transient.

2.3.3. SN 2018lqu/ZTF 18abttsrb

ZTF 18abttsrb (=SN 2018lqu) was first detected in the ZTF difference imaging pipeline on 2018 September 3.13 (MJD = 58,364.13) at J2000 coordinates $\alpha =$ 15:54:11.48 and $\delta =$ +13:30:50.9, at a magnitude of $r = 20.14 \pm 0.33$ mag. The transient was saved as a candidate SN on its second detection on 2018 September 7, and assigned for spectroscopic follow-up. We reported the transient to the TNS on 2019 November 6 (De 2019b), leading to its IAU name of AT 2018lqu. With forced photometry on the ZTF difference images, we found that the transient was not detected on 2018 August 16.17 (MJD = 58,346.17) down to a 5σ limit of $r \approx 21.16$ mag.

The transient was found in the outskirts of WISEA J155413.91+133102.4, an E-type galaxy at $z = 0.035$ (Figure 2), at a projected offset of $\approx 37\farcs1$, corresponding to a physical separation of $\approx$26.7 kpc. We obtained a spectrum of ZTF 18abttsrb with DBSP on 2018 September 12, which exhibited P-Cygni features of He I and Ca II similar to SNe Ib. Subsequent photometry from ZTF and follow-up with P60 + SEDM indicated a faint and fast-evolving (rise time $\lesssim$ 15 days) light curve peaking at an absolute magnitude of $M \approx -16.4$ mag (Figure 3). A nebular-phase spectrum of the source at $\approx$+30 days from the r-band peak with LRIS on the Keck I telescope showed strong [Ca II] and weak [O I] emission lines, confirming an early transition to the nebular phase and the classification of this source as a Ca-rich gap transient.

2.3.4. SN 2018gwo/ZTF 18acbwazl/Gaia 18dfp/PS 19lf

ZTF 18acbwazl (= SN 2018gwo) was first detected in the ZTF difference imaging pipeline on 2018 October 31.49 (MJD = 58,422.49) at J2000 coordinates $\alpha =$ 12:08:38.83 and $\delta =$ +68:46:44.4, at a magnitude of $g = 19.20 \pm 0.17$ mag. Since the source was detected multiple times on the same night as part of the collaboration high-cadence survey, the source was saved to the GROWTH Marshal on 2018 October 31. The source was detected by ZTF after a month-long gap in survey operations due to maintenance on the P48 camera. The source was first detected on 2018 September 28 by Wiggins (2018) at 16.4 mag (clear filter) and reported to the TNS with the IAU name AT 2018gwo, shortly after the sky region emerged from solar conjunction. An upper limit of 17 mag was reported on the previous night. A low-resolution spectrum from the Three Hills Observatory was reported to the TNS on 2018 September 30 and 2018 October 6 by Leadbeater (2018), consistent with an SN Ib/c with a reddened continuum near peak light, causing this source to be renamed SN 2018gwo. Subsequent ZTF photometry showed that the source was detected by ZTF on its post-peak decline tail. We obtained a spectrum of the source

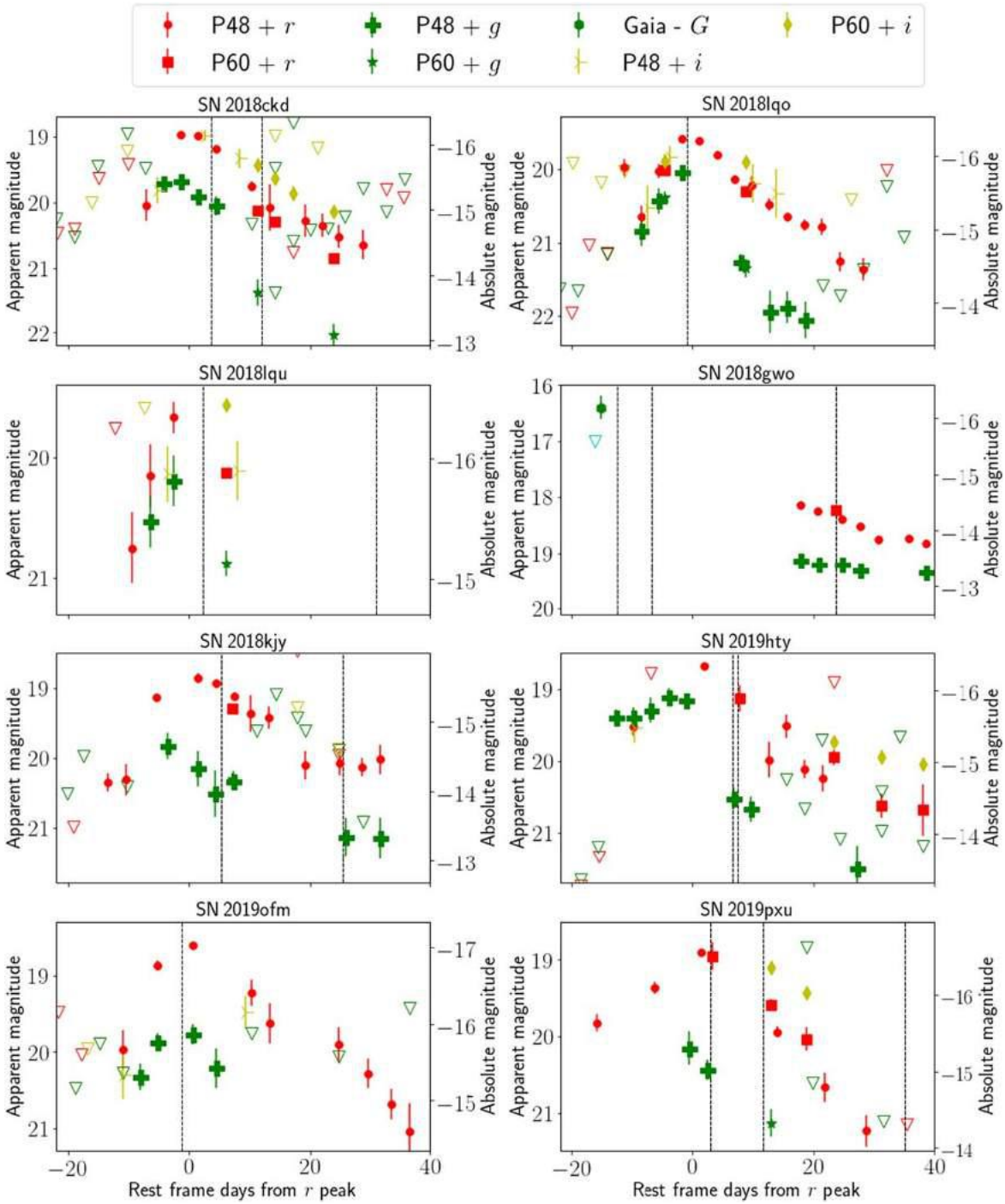

Figure 3. Photometric evolution near peak light of the Ca-rich gap transients presented in this sample, with time presented with respect to the *r*-band light curve of the individual sources (corrected for Galactic extinction). Filled symbols denote detections from forced photometry on the ZTF difference images (see figure legend), while hollow inverted triangles denote 5σ upper limits at the position of the transient. Red points denote *r*-band photometry, green points denote *g*-band photometry, yellow points denote *i*-band photometry, and cyan points denote photometry in the clear filter. The vertical dashed lines denote the epochs of spectroscopy. For SN 2018gwo, we also show public TNS photometry from Gaia & Wiggins (2018) (see legend).

with P60 + SEDM on 2018 November 6, which exhibited a weak continuum with emerging broad [Ca II] and Ca II lines.

The transient was found in the outskirts of NGC 4128, an S0 galaxy at a distance (median reported in NED) of 28.6 Mpc (Figure 2), at a projected offset of $\approx$54.″2 corresponding to a physical projected distance of $\approx$8.6 kpc. Although the transient was not detected by ZTF around peak light, we found the public observations combined with the follow-up to be consistent with a Ca-rich gap transient. First, the initial detection and prior non-detection of the source reported by P. Wiggins suggest a fast rise to an absolute magnitude of $M \approx -16.0$ mag (in clear filter; Figure 3). The transient subsequently declined rapidly by $\approx$2 mag within $\approx$30 days after peak, confirming the faint peak luminosity and fast photometric evolution of the event. The peak light spectra together with the SEDM spectrum taken at $\approx$30 days are

consistent with an SN Ib/c[27] in the photospheric phase, which exhibits a fast transition to the nebular phase. We obtained a follow-up spectrum of the transient with LRIS on the Keck I telescope on 2018 December 04, which exhibited strong [Ca II] emission and weak [O I] emission, confirming the classification of this source as a Ca-rich gap transient.

2.3.5. SN 2018kjy/ZTF 18acsodbf/PS 18cfh

ZTF 18acsodbf (= SN 2018kjy) was first detected in the ZTF difference imaging pipeline on 2018 December 3.36 (MJD = 58,455.36) at J2000 coordinates α = 06:47:17.96 and δ = +74:14:05.9, at a magnitude of $r = 19.56 \pm 0.14$ mag. The transient was saved as a candidate SN on its second detection on 2018 December 4, and assigned for spectroscopic follow-up. The transient was detected by the PS1 survey (Chambers et al. 2016) on 2018 December 17 and reported to the TNS on 2018 December 22 (Chambers et al. 2018), acquiring the IAU name AT 2018kjy. With forced photometry on the ZTF difference images, we found three more lower-significance detections up to ≈7 days before the first alert was issued. The last non-detection of the source was on 2018 November 19.48 (MJD = 58,442.48) to a 5σ limit of $g \approx 20.45$ mag.

The transient was found in the outskirts of NGC 2256, an E-type galaxy at $z = 0.017$ (Figure 2), at a projected offset of ≈17.″2, corresponding to a physical separation of ≈6.4 kpc. We obtained a spectrum of ZTF 18acsodbf with DBSP on 2018 December 14, which exhibited narrow P-Cygni features of He I, O I, and Ca II and a reddened continuum similar to the Ca-rich gap transient PTF 12bho (Lunnan et al. 2017). Subsequent photometry from ZTF and follow-up with P60 + SEDM confirmed a faint and fast-evolving (rise time ≈ 17 days) light curve peaking at an absolute magnitude of $M \approx -15.6$ mag (Figure 3). Subsequent spectra of the source taken with Keck/LRIS +30 days and +120 days from the peak showed a fast transition to the nebular phase dominated by [Ca II] emission, confirming its classification as a Ca-rich gap transient.

2.3.6. SN 2019hty/ZTF 19aaznwze/ATLAS 19nhp/PS 19bhn

ZTF 19aaznwze (= SN 2019hty) was first detected in the ZTF difference imaging pipeline on 2019 June 14.18 (MJD = 58,648.18) at J2000 coordinates α = 12:55:33.03 and δ = +32:12:21.7, at a magnitude of $g = 19.62 \pm 0.19$ mag. The transient passed the machine-learning thresholds on the GROWTH Marshal on 2019 June 20 and was saved for spectroscopic follow-up. The transient was detected by the Asteroid Terrestrial-impact Last Alert System (ATLAS) survey (Tonry et al. 2018) on 2019 June 19 (Tonry et al. 2019a), reported to the TNS on the same date, and assigned the IAU name AT 2019hty. With forced photometry on the ZTF difference images, we found an additional detection of the source on 2019 June 11.24 (MJD = 58,645.24) at a magnitude of $g = 19.52 \pm 0.12$. The last non-detection of the source was on 2019 June 08.23 (MJD = 58,642.23) to a 5σ limit of $r \approx 21.43$ mag.

The transient was found in the outskirts of WISEA J125534.50+321221.5, an E-type galaxy at $z = 0.023$ (Figure 2), at a projected offset of ≈18.″7, corresponding to a physical separation of ≈8.7 kpc. We obtained a spectrum of ZTF 19aaznwze with SEDM and DBSP on 2019 July 1, which exhibited a Type Ib–like spectrum with a reddened continuum and a broad P-Cygni feature of the Ca near-infrared (NIR) triplet. Photometric follow-up with SEDM and data from ZTF showed a faint peak magnitude of $M \approx -16.1$ mag and a rise time of ≈15 days (Figure 3). We obtained an additional spectrum of the source with DBSP at ≈40 days from peak light, which showed a broad emerging line of [Ca II] and weak [O I], confirming a fast transition to the nebular phase dominated by [Ca II] emission, and classifying this source as a Ca-rich gap transient.

2.3.7. SN 2019ofm/ZTF 19abrdxbh/ATLAS 19tjf

ZTF 19abrdxbh (= SN 2019ofm) was first detected in the ZTF difference imaging pipeline on 2019 August 20.15 (MJD = 58,715.15) at J2000 coordinates α = 14:50:54.65 and δ = +27:34:57.6, at a magnitude of $g = 20.43 \pm 0.24$ mag. The transient met the machine-learning thresholds and was saved to the GROWTH Marshal on 2019 August 24. ZTF detection was reported by the AMPEL (Nordin et al. 2019b) automatic stream to the TNS on 2019 August 23 (Nordin et al. 2019a), acquiring for it the IAU name AT 2019ofm. With forced photometry on the ZTF difference images, we found an additional detection of the source on 2019 August 17.24 (MJD = 58,712.24) at a magnitude of $r = 20.07 \pm 0.26$. The last non-detection of the source was on 2019 August 17.15 (MJD = 58,712.15) to a 5σ limit of $g \approx 20.40$ mag.

The transient was found on top of the spectroscopic binary–type galaxy IC 4514 at $z = 0.030$ (Figure 2), at a projected offset of ≈18.″2, corresponding to a physical offset of ≈11.2 kpc. We obtained a spectrum of the source with DBSP on 2019 August 27, which exhibited clear features of a 1991bg-like SN Ia at the host redshift. Following the first detection, the source rose to a peak absolute magnitude of $M_r \approx -16.6$ mag, suggesting a subluminous SN Ia consistent with the spectroscopic classification. We obtained a follow-up spectrum of the source with LRIS at ≈175 days after peak light, which showed that the source had transitioned to the nebular phase exhibiting [Ca II] as the only detectable broad feature in the spectrum. Together with the non-detection of Fe-group features typically seen in 1991bg-like objects, the strong [Ca II] feature suggested that SN 2019ofm was similar to the Ca-rich gap transients PTF 09dav and SN 2016hnk, thus classifying the source as a Ca-rich gap transient.

2.3.8. SN 2019pxu/ZTF 19abwtqsk/ATLAS 19uvg/PS 19fwq

ZTF 19abwtqsk (=SN 2019pxu) was first detected in the ZTF difference imaging pipeline on 2019 September 4.50 (MJD = 58,730.50) at J2000 coordinates α = 05:10:12.61 and $\delta = -00{:}46{:}38.6$, at a magnitude of $r = 20.09 \pm 0.20$ mag. The transient met the machine-learning thresholds and was saved to the GROWTH Marshal on 2019 September 22 on its third detection in the ZTF alert stream. The transient was detected by the ATLAS survey on 2019 September 10 (Tonry et al. 2019b) and reported on the same date to the TNS, acquiring the IAU name AT 2019pxu. The field was not covered by the survey >30 days before the first detection, and hence we were unable to determine a recent upper limit from the first detection.

[27] Although not used as a defining characteristic of the class, the only SNe Ib/c reported thus far in the outskirts of early-type galaxies are found to be Ca-rich gap transients.

Table 2
Photometry of All the Sources Presented in This Paper

Object	MJD	Rest-frame Phase (days from r peak)	Filter	Magnitude	Instrument
SN 2018ckd	58,242.31	−34.53	r	>20.53	P48+ZTF
SN 2018ckd	58,245.34	−31.57	r	>18.89	P48+ZTF
SN 2018ckd	58,248.27	−28.71	r	>20.95	P48+ZTF
SN 2018ckd	58,255.26	−21.88	r	>20.70	P48+ZTF
SN 2018ckd	58,258.25	−18.96	r	>20.64	P48+ZTF
SN 2018ckd	58,262.30	−15.01	r	>19.87	P48+ZTF
SN 2018ckd	58,267.31	−10.12	r	>19.65	P48+ZTF
SN 2018ckd	58,270.32	−7.18	r	20.28 ± 0.24	P48+ZTF
SN 2018ckd	58,276.19	−1.45	r	19.21 ± 0.03	P48+ZTF
SN 2018ckd	58,279.17	1.46	r	19.23 ± 0.04	P48+ZTF
SN 2018ckd	58,282.19	4.41	r	19.42 ± 0.04	P48+ZTF
SN 2018ckd	58,285.17	7.32	r	>18.28	P48+ZTF
SN 2018ckd	58,288.24	10.32	r	19.99 ± 0.08	P48+ZTF
SN 2018ckd	58,289.23	11.29	r	20.36 ± 0.07	P60+SEDM
SN 2018ckd	58,291.24	13.25	r	20.32 ± 0.35	P48+ZTF
SN 2018ckd	58,292.25	14.24	r	20.54 ± 0.09	P60+SEDM
SN 2018ckd	58,295.24	17.16	r	>21.00	P60+SEDM
SN 2018ckd	58,297.27	19.14	r	20.52 ± 0.25	P48+ZTF
SN 2018ckd	58,300.18	21.98	r	20.59 ± 0.18	P48+ZTF
SN 2018ckd	58,302.25	24.00	r	21.08 ± 0.07	P60+SEDM

Notes. The photometry has not been corrected for Galactic extinction. Phases are indicated with respect to the time from the best-fit r-band peak. Upper limits are at 5σ confidence at the location of the transient.

(This table is available in its entirety in machine-readable form.)

The transient was found in the outskirts of the spiral galaxy WISEA J051011.32-004702.5 at $z = 0.028$, at a projected offset of $\approx 30\farcs9$ (Figure 2), corresponding to a physical projected offset of ≈17.6 kpc. We obtained a peak light spectrum of the source with P200 + DBSP on 2019 October 3, which exhibited a Type Ib–like spectrum and a reddened continuum similar to the Ca-rich gap transient PTF 12bho. Subsequent photometry from ZTF and P60 + SEDM indicated a rise time of ≈17 days and a faint peak absolute magnitude of $M = -16.4$ mag. We obtained a follow-up spectrum with LRIS on 2019 October 27, which showed a faint continuum with emerging broad emission lines of [Ca II] and Ca II, confirming a fast nebular transition and the classification of the source as a Ca-rich gap transient.

2.4. Photometry

We obtained *gri* photometry of the transients from data taken with the P48 ZTF camera (Bellm et al. 2019a), which were processed with the ZTF data processing system (Masci et al. 2019). Light curves were extracted using forced point-spread function (PSF) photometry (Masci et al. 2019) at the location of the transient in the difference images, where the location was determined from the median position of the source reported in all alerts of the transient in the ZTF transient detection pipeline. We report detections of the transients in the forced photometry for epochs where the signal-to-noise ratio (S/N) was higher than 3σ, while 5σ upper limits are reported for other epochs. We include data acquired in the public survey as well as those acquired in the higher-cadence internal collaboration and Caltech surveys. In cases where the transient was covered by an internal survey and had more than one visit per night, we performed an inverse variance weighted binning of the flux measurements in bins of 2.5 days to improve the S/N of the measurements. We performed the same binning for reporting upper limits, where we used the inverse variance weighted flux uncertainty to report the 5σ upper limit for that epoch.

We obtained additional multi-color photometry near peak light with the SEDM rainbow camera on the Palomar 60 inch telescope, and the data were processed using the SEDM image reduction pipeline. Image subtraction against archival references from the Sloan Digital Sky Survey (SDSS) and PS1 was performed, and difference magnitudes were obtained using the pipeline described in Fremling et al. (2016). We show the photometric evolution of these transients near peak light in Figure 3, while the data are presented in Table 2. We corrected the photometry for foreground Galactic extinction using the maps in Schlafly & Finkbeiner (2011) and the extinction law of Cardelli et al. (1989), assuming $R_V = 3.1$.

2.5. Late-time Imaging

We obtained additional late-time photometry of the transients with the Wafer-scale Imager for Prime (WaSP) on the Palomar 200 inch telescope, which was reduced with the pipeline described in De et al. (2020). We used LRIS on the Keck I telescope for late-time imaging of some transients reported in this paper, and the data were reduced using the automated `lpipe` pipeline (Perley 2019). Image subtraction was not necessary for the late-time imaging for most sources since the majority were far from their host galaxies, and we report aperture photometry measurements (accounting for aperture corrections) for these sources, calibrated against the PS1 (Chambers et al. 2016) catalog.

For sources whose photometry was deemed to be contaminated by host galaxy light from visual inspection (which was found to be true only for SN 2018kjy), we performed image subtraction using reference images from WaSP obtained >1 year after the peak of the transient light curve. The image subtraction was performed by first aligning the science image

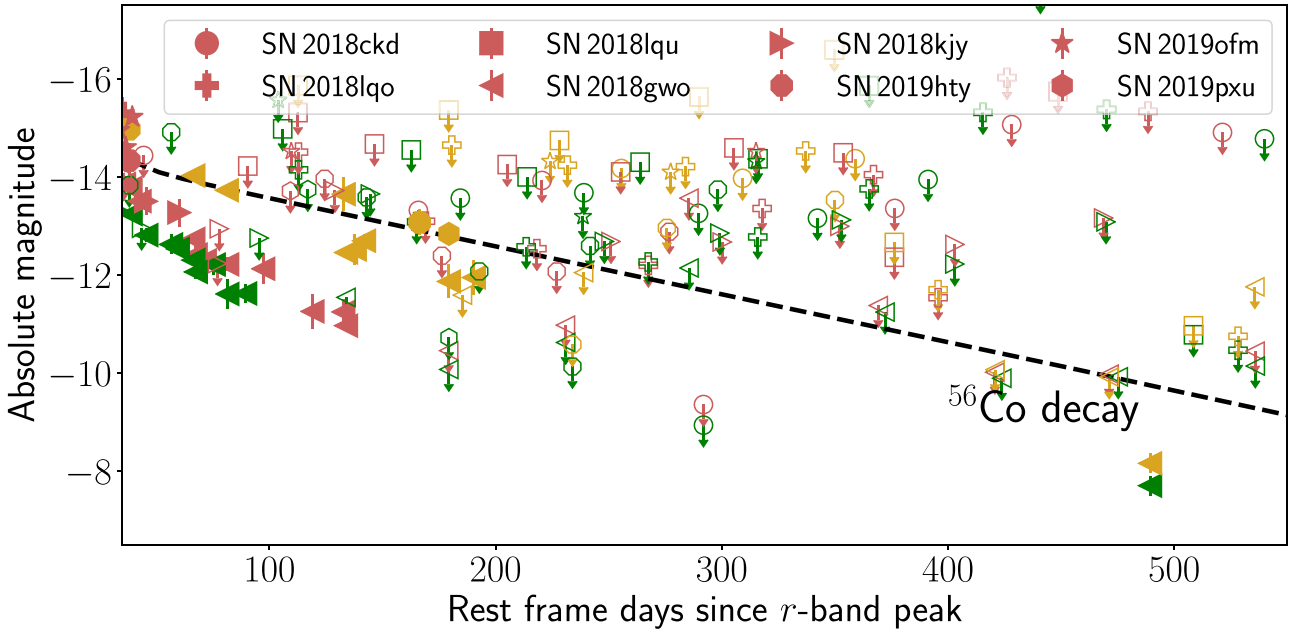

Figure 4. Late-time photometric evolution of the Ca-rich gap transients in the CLU sample, as a function of rest-frame time from the *r*-band peak. Each object is assigned a separate symbol for late-time detections as indicated in the legend. The colors denote individual filters: brown for the *r* band, light green for the *g* band, and gold for the *i* band. Upper limits are indicated as hollow symbols with arrows in the respective filter colors. The black dashed line shows the decline rate expected from the radioactive decay of ^{56}Co using an Arnett model with a ^{56}Ni mass of 0.015 $M_{\odot}$, under the assumption of complete trapping of γ-rays.

to the reference image by aligning the two images to the same system calibrated against Gaia DR2 (Gaia Collaboration et al. 2018). The alignment was performed by first extracting a source catalog for both the science and the reference image using `SExtractor` (Bertin 2006) followed by astrometric alignment using the `scamp` code with Gaia DR2 as the reference catalog.

The images were then resampled to the same output grid using `Swarp` (Bertin et al. 2002) and flux-scaled to a common zero-point. Image subtraction was performed using the `ZOGY` code (Zackay et al. 2016) using an input PSF model for the science and reference image using `PSFEx` (Bertin 2011). Forced PSF photometry was performed on the generated difference image to estimate the flux and flux uncertainty at the transient position, including an additional Monte Carlo simulation of the PSF-fit flux variance across the difference images to account for uncorrected correlated noise in the difference image output.

However, we caution that in several cases, the latest images from LRIS showed evidence of diffuse sources near the transient, which we were unable to subtract due to the absence of a template (ideally acquired several hundred days after the latest observation), and thus report the host-contaminated aperture photometry fluxes only. As in the case of the ZTF photometry, we report detections of sources whose S/N was higher than 3σ, and detections with 5σ upper limits. The late-time photometric evolution for the sample is shown in Figure 4. We discuss the local environments of the Ca-rich gap transients as observed in the late-time imaging in Section 4.2.

2.6. Spectroscopy

Spectroscopic follow-up of transients near peak light was obtained as a part of the regular classification effort of the CLU experiment. Typically one spectrum was obtained near peak light for initial spectroscopic classification and a sequence of nebular-phase spectra were obtained starting at least ≈30 days after peak. The SEDM spectrograph was used for spectroscopy for only two of these sources (SN 2018gwo and SN 2019hty) since they were typically too faint (>19 mag) for SEDM spectroscopy. The SEDM data were reduced using the `pysedm` (Rigault et al. 2019) automatic pipeline. Peak light spectroscopy for the rest of the sample was obtained using the DBSP, and the data were reduced using the `pyraf-dbsp` pipeline (Bellm & Sesar 2016).

We obtained two epochs of spectroscopy of SN 2018gwo with the APLY200 spectrograph at Three Hills Observatory. The spectra were reduced using ISIS software.[28] The spectrum images were bias- and dark-subtracted, flat-field corrected using a tungsten halogen lamp, corrected for geometric distortions, and sky background subtracted before extracting the spectrum profile. The spectrum was wavelength-calibrated using an Ne/Ar reference lamp and calibrated in relative flux using as a reference, a hot star (HD 123299) from the MILES library of spectra[29] measured the same night at similar airmass. We obtained follow-up spectroscopy for some sources using the Alhambra Faint Object Spectrograph and Camera (ALFOSC) on the Nordic Optical Telescope (NOT). The NOT data were reduced using the FOSCGUI pipeline.[30]

Late-time nebular spectroscopy was obtained using LRIS on the Keck I telescope starting from ≈30 days after peak light. For some sources, we obtained up to four epochs of nebular-phase spectra using LRIS. The data were reduced using the automated `lpipe` pipeline. We present the complete list of spectroscopic observations in Table 3, while the spectra are presented in Figure 5. In addition, we used publicly available spectra from the TNS for SN 2018gwo and some events in the control sample (Appendix). Spectra for the literature sample of events were obtained from WISeREP (Yaron & Gal-Yam 2012) and

[28] By C. Buil; http://www.astrosurf.com/buil/isis-software.html.
[29] http://miles.iac.es/
[30] http://graspa.oapd.inaf.it/foscgui.html

Table 3
Log of Spectroscopic Observations of All Objects Presented in This Paper

Object	Observation Date (UTC)	MJD	Phase (days from r peak)	Telescope + Instrument	Range Å	Resolution $\lambda/\delta\lambda$
SN 2018ckd	2018-06-12	58,281.3	+3	P200 + DBSP	3500–10000	1000
SN 2018ckd	2018-06-21	58,290.2	+12	P200 + DBSP	3500–10000	1000
SN 2018ckd	2018-08-08	58,338.3	+57	Keck I + LRIS	3500–10000	1000
SN 2018ckd	2019-04-03	58,576.5	+291	Keck I + LRIS	3500–10000[†]	1000
SN 2018lqo	2018-08-21	58,351.2	−1	P200 + DBSP	3500–10000	1000
SN 2018lqo	2018-10-12	58,403.3	+49	Keck I + LRIS	3500–10000	1000
SN 2018lqu	2018-09-12	58,373.1	+2	P200 + DBSP	3500–10000	1000
SN 2018lqu	2018-10-12	58,403.2	+31	Keck I + LRIS	3500–10000	1000
SN 2018gwo	2018-09-30	58,391.8	−12	THO + ALPY	3700–7500	100
SN 2018gwo	2018-10-06	58,397.8	−6	THO + ALPY	3700–7500	100
SN 2018gwo	2018-11-06	58,428.5	+23	P60 + SEDM	3800–9200	100
SN 2018gwo	2018-12-04	58,456.6	+51	Keck I + LRIS	3500–10000	1000
SN 2018gwo	2019-03-07	58,549.5	+143	Keck I + LRIS	3500–10000	1000
SN 2018gwo	2019-06-03	58,637.3	+230	Keck I + LRIS	3500–10000	1000
SN 2018kjy	2018-12-14	58,466.3	+5	P200 + DBSP	3500–10000	1000
SN 2018kjy	2019-01-04	58,487.4	+25	Keck I + LRIS	3500–10000	1000
SN 2018kjy	2019-04-03	58,576.2	+113	Keck I + LRIS	3500–10000	1000
SN 2019hty	2019-07-01	58,665.2	+6	P200 + DBSP	3500–10000	1000
SN 2019hty	2019-07-02	58,666.2	+7	P60 + SEDM	3800–9200	100
SN 2019hty	2019-08-04	58,699.2	+40	P200 + DBSP	3500–10000	1000
SN 2019ofm	2019-08-27	58,722.3	−1	P200 + DBSP	3500–10000	1000
SN 2019ofm	2020-02-18	58,897.5	+168	Keck I + LRIS	3500–10000	1000
SN 2019pxu	2019-09-24	58,750.4	+3	P60 + SEDM	3800–9200	100
SN 2019pxu	2019-10-03	58,759.5	+11	P200 + DBSP	3500–10000	1000
SN 2019pxu	2019-10-27	58,783.5	+35	Keck I + LRIS	3500–10000	1000
SN 2019pxu	2020-02-18	58,897.3	+146	Keck I + LRIS	3500–10000	1000
SN 2018dbg	2018-08-04	58,334.0	+22	P200 + DBSP	3500–10000	1000
SN 2018fob	2018-08-21	58,351.0	−8	P200 + DBSP	3500–10000	1000
SN 2018fob	2018-08-31	58,361.0	+0	P60 + SEDM	3800–9200	100
SN 2018fob	2019-04-03	58,576.0	+209	Keck I + LRIS	3500–10000	1000
SN 2018kqr	2018-12-14	58,466.3	+1	P200 + DBSP	3500–10000	1000
SN 2018kqr	2018-12-27	58,479.2	+14	P200 + DBSP	3500–10000	1000
SN 2019yz	2019-02-20	58,534.2	+7	NOT + ALFOSC	3800-9500	300
SN 2019yz	2019-04-15	58,588.2	+61	P60 + SEDM	3800–9200	100
SN 2019yz	2019-06-08	58,642.0	+114	P60 + SEDM	3800–9200	100
SN 2019yz	2019-07-02	58,666.0	+138	P60 + SEDM	3800–9200	100
SN 2019yz	2019-09-26	58,752.2	+224	Keck I + LRIS	3500–10000	1000
SN 2019abb	2019-01-26	58,509.2	−4	P200 + DBSP	3500–10000	1000
SN 2019abb	2019-02-09	58,523.0	+9	P60 + SEDM	3800–9200	100
SN 2019abb	2019-02-10	58,524.9	+11	NOT + ALFOSC	3800–9500	300
SN 2019abb	2019-04-06	58,579.2	+64	Keck I + LRIS	3500–10000	1000
SN 2019abb	2020-01-24	58,872.0	+353	Keck I + LRIS	3500–10000	1000
SN 2019ape	2019-02-12	58,526.4	−13	P200 + DBSP	3500–10000	1000
SN 2019ape	2019-03-01	58,543.1	+2	NOT + ALFOSC	3800–9500	300
SN 2019ape	2019-12-03	58,820.0	+274	Keck I + LRIS	3500–10000	1000
SN 2019ccm	2019-04-06	58,579.2	+6	Keck I + LRIS	3500–10000	1000
SN 2019ccm	2019-09-28	58,754.0	+178	Keck I + LRIS	3500–10000	1000
SN 2019txl	2019-04-06	58,579.0	+11	Keck I + LRIS	3500–10000	1000
SN 2019txl	2020-02-18	58,897.0	+318	Keck I + LRIS	3500–10000	1000
SN 2019txr	2019-06-04	58,638.0	+28	Keck I + LRIS	3500–10000	1000
SN 2019txr	2020-02-18	58,897.0	+276	Keck I + LRIS	3500–10000	1000
SN 2019txt	2019-05-13	58,616.0	+10	P200 + DBSP	3500–10000	1000
SN 2019txt	2019-06-04	58,638.0	+31	Keck I + LRIS	3500–10000	1000
SN 2019txt	2020-01-24	58,872.0	+259	Keck I + LRIS	3500–10000	1000
SN 2019gau	2019-06-04	58,638.9	−4	P60 + SEDM	3500–10000	100
SN 2019gau	2020-02-18	58,897.0	+260	Keck I + LRIS	3500–10000	1000
SN 2019gsc	2019-06-04	58,638.2	−2	P200 + DBSP	3500–10000	1000
SN 2019gsc	2019-07-04	58,668.0	+27	Keck I + LRIS	3500–10000	1000
SN 2019ttf	2019-07-04	58,668.0	+10	Keck I + LRIS	3500–10000	1000
SN 2019ttf	2020-03-22	58,930.0	+269	Keck I + LRIS	3500–10000	1000
SN 2019mjo	2019-08-01	58,696.0	+7	P200 + DBSP	3500–10000	1000
SN 2019mjo	2020-01-24	58,872.0	+176	Keck I + LRIS	3500–10000	1000

Table 3
(Continued)

Object	Observation Date (UTC)	MJD	Phase (days from r peak)	Telescope + Instrument	Range Å	Resolution $\lambda/\delta\lambda$
SN 2019ouq	2019-08-04	58,699.3	+6	P200 + DBSP	3500–10000	1000
SN 2019ouq	2020-01-24	58,872.0	+173	Keck I + LRIS	3500–10000	1000

Note. † denotes spectra that do not have high enough S/N to detect features.

attributed to the original source where relevant. All data presented in this paper will be publicly released on WISeREP and as an electronic supplement upon publication.

3. Analysis of the Combined Sample

Here, we present a combined analysis of the spectroscopic and photometric properties of the sample of Ca-rich gap transients presented in this paper and those of the literature sample of events that satisfy our selection criteria. We begin with a qualitative analysis of the spectroscopic properties, particularly to highlight the existence of a continuum of spectroscopic characteristics in the full sample of events. We outline the procedures used for a quantitative analysis of the full sample of events, and present quantitative results on the photometric and spectroscopic properties of the sample to highlight trends across the continuum of spectroscopic properties. We use these results to discuss implications for the progenitor channels in Section 6.

3.1. Photospheric-phase Spectra

Since we aim to characterize the peak light spectral diversity in this section, we discuss objects for which a medium-resolution spectrum was available within ≈10 days of peak light—16 of the total sample of 18 objects[31] have photospheric-phase spectra acquired near the peak of the light curve. The photospheric-phase spectra of this sample are diverse, and most notably separate into SN Ib/c–like (absence of a strong Si II line, with a continuum of He I line strengths) and SN Ia–like (with strong Si II lines) objects. This distinction is a natural parallel to the traditional classification scheme invoked for the broader population of hydrogen-poor SNe (Filippenko 1997; Gal-Yam 2017). We thus proceed by defining two spectroscopic classes within the sample of Ca-rich gap transients based on their similarity to either SNe Ib/c or SNe Ia near peak light and refer to them as Ca-Ib/c and Ca-Ia objects. Within the photometric selection criteria defined in this experiment, the relative occurrence rate of the Ca-Ib/c to the Ca-Ia objects is 6:1, although a true-rate estimate would require incorporating the luminosity functions of the two classes (see Section 5).

3.1.1. The Ca-Ib/c Class

In Figure 6, we plot the photospheric-phase spectra of the Ca-Ib/c objects. Prominent spectral lines detected in the photospheric phase are marked, along with three optical lines of He I and their P-Cygni absorption regions due to the known similarity of these objects to SNe Ib at peak (Perets et al. 2010). The ZTF sample of events is dominated by Type Ib–like spectra near peak light (exhibiting He I λ5876, λ6678, and λ7065) in the photospheric-phase spectra albeit with a range of line strengths and velocities. The He I λ6678 line is usually contaminated by the nearby Si II $\lambda\lambda$6347, 6371 lines (Sullivan et al. 2011; Kasliwal et al. 2012; De et al. 2018a). Other common features in the peak light spectra include P-Cygni features of O I λ7774 and Ca II H&K and the NIR triplet. SN 2012hn is the only object that does not show any evidence of He I in its peak spectrum (Valenti et al. 2014). We also do not conclusively identify He I in the peak light spectrum of SN 2018gwo. We thus tentatively classify SN 2018gwo as a Ca-Ic although the low S/N and resolution of the peak spectrum preclude a definite classification.

Upon closer inspection, the set of peak light spectra shown in Figure 6 is demarcated into two groups of events—one with events characterized by flat continua across the entire spectral range and one with events characterized by strong suppression of flux at bluer wavelengths and red continua. We indicate these two classes of events with different colors (dark green and red) in Figure 6, and throughout the rest of this manuscript. The spectra of events in the first class are relatively homogeneous, and show clear evidence of strong He I at normal photospheric velocities (≈8000–11,000 km s^{-1}; see Section 3.1.3). Notably, these objects exhibit a strong continuum in the blue side of the spectrum (below 5500 Å) and clear absorption features of Ca II, Mg I and Fe II superimposed on the blue-side continuum.

On the other hand, events in the latter group show strong suppression of the continuum flux in the blue side of the spectrum (below 5500 Å) producing a spectrum with redder colors. These exhibit a diverse range of line velocities, ranging from events with normal photospheric velocities (SN 2019pxu) to peculiar low-velocity (≈4000–6000 km s^{-1}) events such as PTF 12bho and SN 2018kjy. Absorption features of metals blueward of 5500 Å (Ca II, Mg I, and Fe II) are only weakly detected due to the strong suppression of flux in this region. Notably, SN 2012hn and SN 2018gwo in this group do not show evidence of He I (and hence would be Ca-Ic objects nominally), while SN 2018kjy exhibits only weak signatures of low-velocity He I in its spectrum. Given the small number of events, it is unclear whether there is a continuum of events between these two types of objects. We proceed by referring to the two classes of objects as objects with green and red continua respectively, and use the same color scheme as in Figure 6.

There is considerable diversity in the presence and strength of He lines in the peak light spectra of the Ca-Ib/c objects. The identification of He is a crucial aspect for understanding the progenitors of these explosions since the presence of He in the ejecta is indicative of an He-rich progenitor system. However, He lines visible in the optical region are non-thermally excited (Dessart et al. 2012; Hachinger et al. 2012) and hence their absence does not necessarily preclude the presence of He in the ejecta. The detection of He lines is dependent on the amount of

[31] SN 2007ke and PTF 11bij are the only objects that do not have a peak light spectrum.

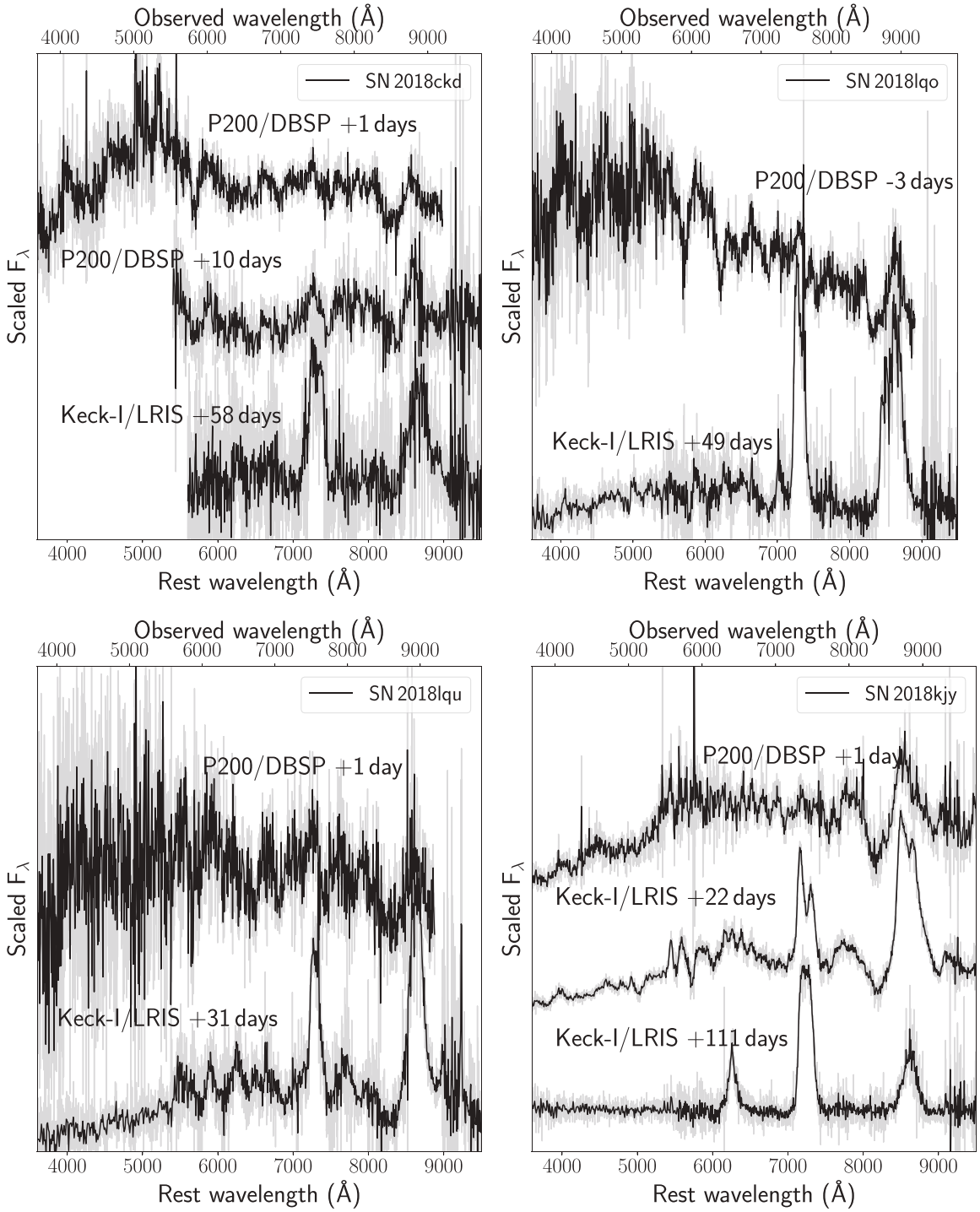

Figure 5. Spectroscopic sequence of the sample of Ca-rich gap transients presented in this paper. In each panel, the object name is indicated in the legend and the phase of the spectrum is denoted next to each spectrum with respect to the peak of the *r*-band light curve. The gray lines show the unbinned spectra while the black lines show the same spectra binned to improve the S/N.

(The data used to create this figure are available.)

^{56}Ni mixing in the ejecta, since ^{56}Ni is able to excite He I transitions non-thermally. Thus, the presence of He lines also constrain the radioactive mixing in the ejecta. While most of the Ca-Ib/c objects exhibit prominent and unambiguous He I lines in the optical, similar to the prototype event SN 2005E, these lines are difficult to unambiguously identify in peculiar events.

In Figure 7, we show zoomed-in regions of the peak light spectra of the sample around the optical He I lines at 5876 Å, 6678 Å and 7065 Å. The identification of He is complicated by the contamination of the He I 5876 Å line with the nearby Na I line seen in SNe Ic, thus requiring the detection of multiple He I lines at similar velocities to conclusively confirm the presence of He. This necessitates a careful examination of the features

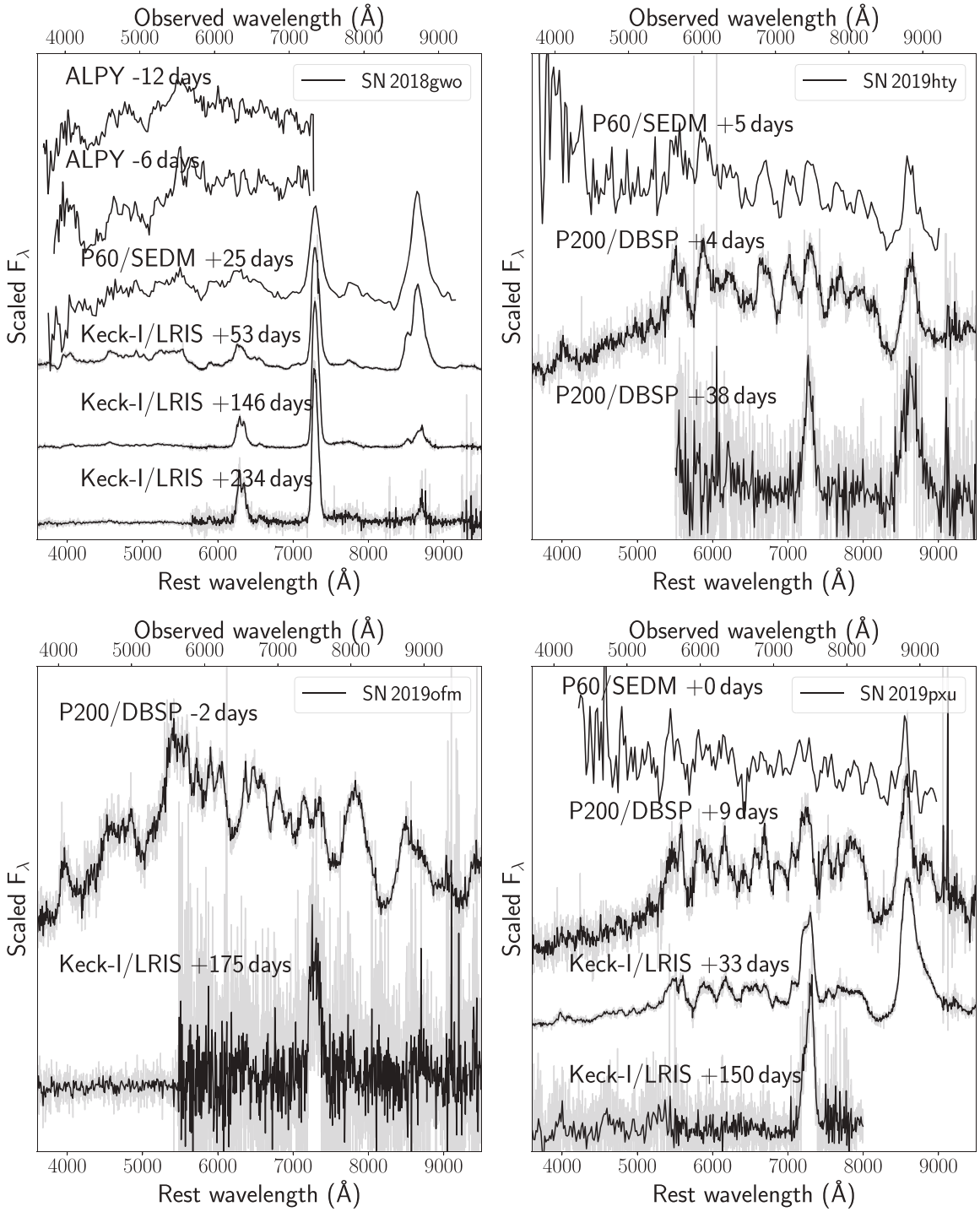

Figure 5. (Continued.)

around the other optical He I lines at 6678 Å and 7065 Å. We note that all the green Ca-Ib/c events exhibit unambiguous evidence of He I at similar velocities at all the optical transitions.

However, the family of events with red continua exhibit much more diverse properties around the He I transitions, which include peculiar events like SN 2012hn, PTF 12bho and SN 2018kjy. Only SN 2019hty exhibits unambiguous P-Cygni absorption in all the He I lines and thus He can be confirmed. In the progression from SN 2019pxu to SN 2012hn, we see a gradual change in the strength and absorption depth of the He lines. Specifically, we note the appearance of an emission feature at the expected absorption position of the He I λ7065 line that gets stronger from SN 2019pxu to SN 2012hn. This emission feature has been attributed to C II in the spectral modeling of SN 2012hn, although it could also be associated with Al II (Kasliwal et al. 2010; Sullivan et al. 2011; De et al. 2018a). In the same sequence of objects the He I λ7065 line gets progressively weaker until it is not detected at all in SN 2012hn. The same trend is also detected in the He I λ6678 line although the identification of He I λ6678 in SN 2012hn is

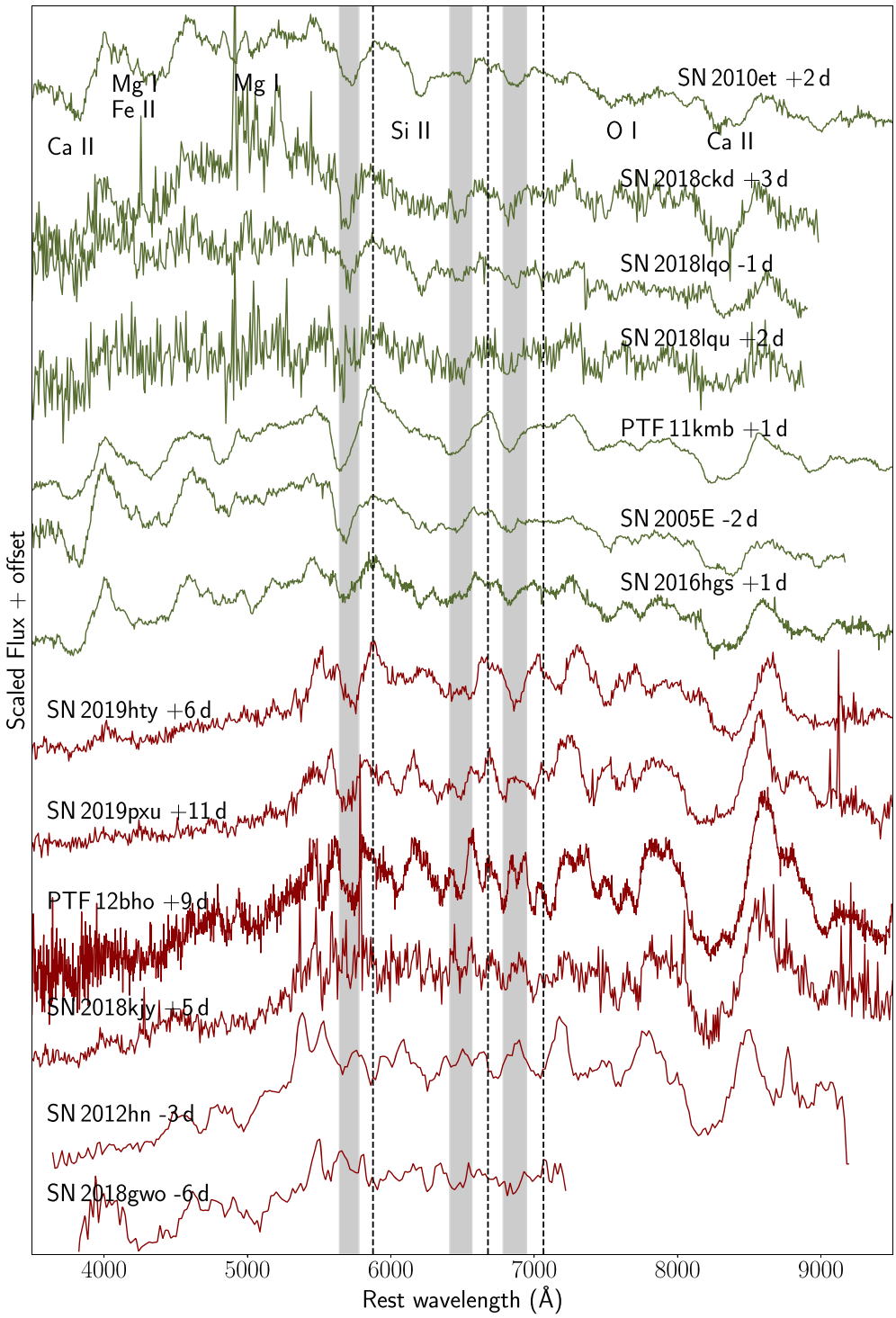

Figure 6. Photospheric-phase spectra of Ca-rich gap transients that exhibit SN Ib/c–like features (termed Ca-Ib/c objects) in the ZTF sample combined with the same for events in the literature. The transient name and phase of the spectrum are indicated next to each spectrum. The spectrum color separates the two primary spectral types in the sample based on the shape of the continuum—the events plotted in green have peak spectra characterized by flat or green continua, while spectra in red show events that exhibit strong suppression of flux at bluer wavelengths thus exhibiting red continua. The dashed lines show the rest-frame wavelengths of three optical He I lines, while the shaded bars show the expected P-Cygni absorption minima for velocities ranging from 5000 to 12,000 km s^{-1}.

complicated by the presence of the nearby Si II line. SN 2012hn does not show any evidence of He either in its optical or in its NIR spectra (Valenti et al. 2014). We thus find evidence of a continuum of He line strengths in these events, which range from events with strong He lines to those with very weak or absent He lines.

3.1.2. The Ca-Ia Class

Figure 8 shows a comparison of the photospheric- and nebular-phase spectra of the three Ca-Ia objects in the sample, indicated by orange markers throughout this manuscript. These objects exhibit the typical features of 1991bg-like objects defined by a strong Ti II trough in the blue side of the spectrum.

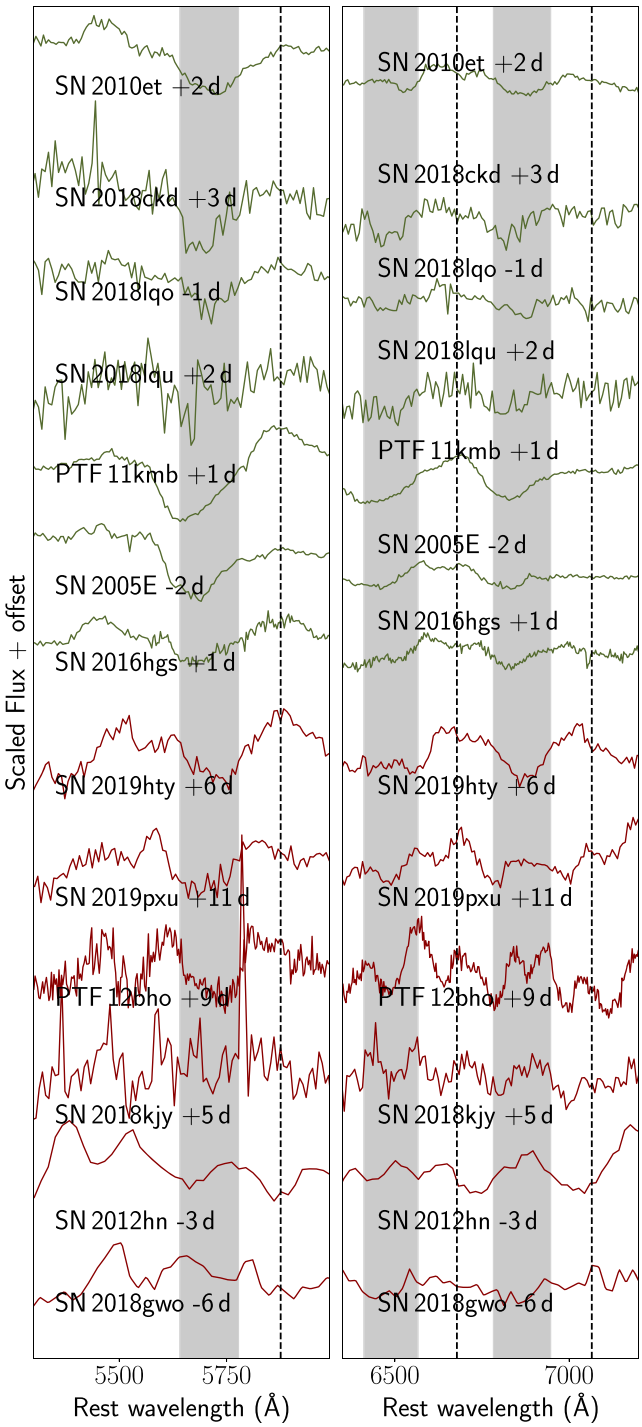

Figure 7. Zoomed-in plots of the photospheric-phase spectra of the Ca-Ib/c objects around the expected positions of He I transitions. The left panel shows the region around the He I λ5876 line and the right panel shows the region including the He I λ6678 and λ7065 lines. The color coding of the spectra is the same as that in Figure 6. The black dashed lines show the rest-frame positions of the He I lines, while the gray shaded regions show the absorption region for the velocity range of 5000–12,000 km s^{-1}.

In addition, all of these objects exhibit mild to strong line blanketing features shortward of 5000 Å in the blue side of the spectrum. Such features are typically indicative of the outer ejecta being rich in Fe-group material that efficiently absorbs the blue flux (Nugent et al. 1997; Polin et al. 2019a). We note that SN 2019ofm exhibits several similarities to the peak light spectrum of SN 2016hnk (although with lower line velocities), while PTF 09dav exhibits some different features and line strengths, some of which were attributed to rare elements like Sc II and Sr II in Sullivan et al. (2011). Although the peak light spectra are broadly similar, such exotic elements were not required in the spectral modeling of SN 2016hnk in Galbany et al. (2019) and Jacobson-Galán et al. (2020), and hence are unlikely for SN 2019ofm given the spectral similarity between the two objects.

Given the lack of prominent He lines in both the Ca-Ic objects and Ca-Ia objects, it is instructive to compare the peak light spectra of the two classes. In Figure 9, we plot the peak light spectrum of SN 2012hn—the only unambiguous Ca-Ic object in the sample—along with the peak light spectra of two Ca-Ia objects, SN 2019ofm and SN 2016hnk. It is worth noting the striking resemblance between the spectra of SN 2012hn and SN 2019ofm, barring the weaker strength of the Si II line in SN 2012hn (which leads to its Ca-Ic classification). Specifically, we find that although the velocities are different in the three objects, they show similar features over the entire optical spectrum. The only discrepancies are in the bluer part of the spectrum where the Ca-Ia objects show features from Fe-group elements (near ≈4000 Å). SN 2016hnk exhibits a very strong Si II line similar to normal/subluminous SNe Ia (Gal-Yam 2017), while SN 2019ofm exhibits a weaker Si II line but with all the characteristic SN Ia features, and SN 2012hn exhibits the weakest Si II line and nearly the same spectral features as SN 2019ofm.

Sun & Gal-Yam (2017) demonstrated that SN I subtypes (Ia/Ib/Ic) occupy different loci on the line depth diagram of Si II λ6150 Å and O I λ7774 Å measured in peak-brightness spectra (see their Figure 9). In order to quantitatively investigate the striking similarities between the Ca-Ia and Ca-Ic objects, we performed these measurements in a manner similar to that of Sun & Gal-Yam (2017). SN 2016hnk exhibits a λ6150 line depth of ≈0.6 and a depth ratio of $\lambda6150/\lambda7774 \approx 0.75$, similar to 91bg-like SNe Ia in the Sun & Gal-Yam (2017) sample. However, we find that SN 2019ofm exhibits a λ6150 line depth of ≈0.35 and a depth ratio of $\lambda6150/\lambda7774 \approx 0.83$ and is exactly at the SN Ia–SN Ic classification boundary suggested in that work.

Similarly, the peak spectrum of SN 2012hn exhibits a λ6150 depth of ≈0.3 and a depth ratio of $\lambda6150/\lambda7774 \approx 1.0$, which falls exactly on the classification boundary for SNe Ib/c in that sample. In particular, we note that SN 2019ofm and SN 2012hn occupy an empty phase space in the classification diagram of Sun & Gal-Yam (2017)—with SN 2019ofm being a transitional Ia–Ic object and SN 2012hn being a transitional Ib–Ic object. We thus conclude that there may be a continuum of events from Ca-Ia to Ca-Ic to Ca-Ib objects based on their peak light photospheric spectral properties. We discuss this sequence together with the photometric- and nebular-phase properties in Section 6.

3.1.3. Photospheric Velocities

For a quantitative comparison of the spectral features, we performed fits of the most prominent spectroscopic features of the combined sample of events, and list the derived parameters in Table 4. The aim of this exercise is to elucidate the photospheric velocity evolution of the most prominent spectral lines in these transients as they hold clues to the density structure of the ejecta and internal emission powering

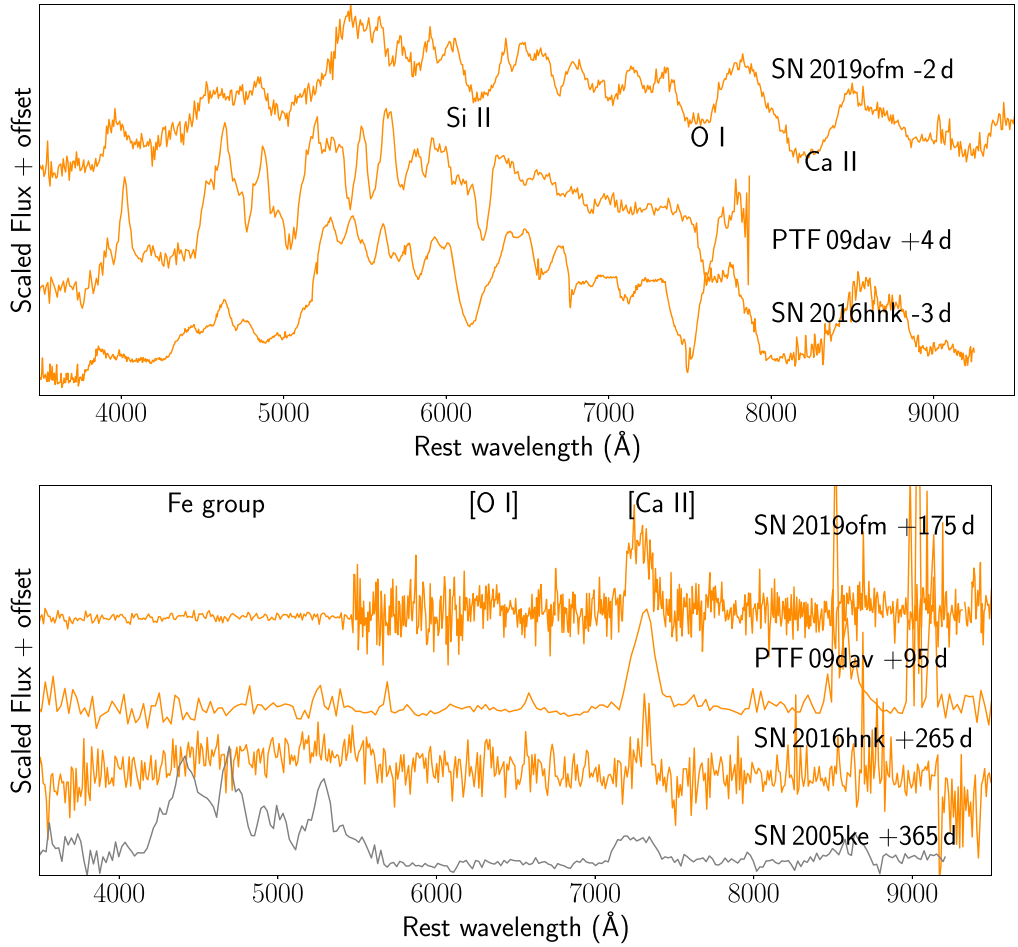

Figure 8. Photospheric-phase (top panel) and nebular-phase (bottom panel) spectra of Ca-rich gap transients that exhibit SN Ia–like features (termed Ca-Ia objects) in the ZTF sample combined with the same for events in the literature. The transient name and phase of the spectrum are indicated next to each spectrum. The prominent photospheric lines of Si II, O I, and Ca II are marked in the peak light spectra plot while the nebular lines of [O I], [Ca II], and Fe-group elements are marked in the lower panel. In the lower panel, we also show a nebular-phase spectrum of the SN 1991bg–like event SN 2005ke to highlight the differences between 1991bg-like objects and Ca-rich objects in terms of the absence of Fe-group features in the blue part of the spectrum.

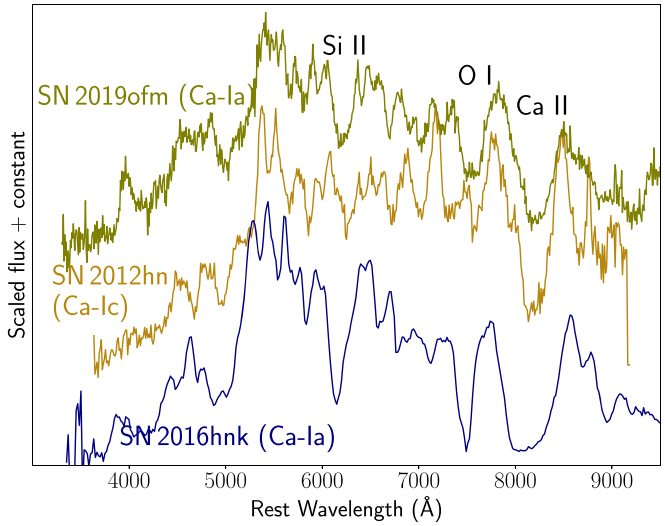

Figure 9. Comparison of the peak light optical spectra of He-poor Ca-Ib/c event SN 2012hn and the two Ca-Ia events SN 2016hnk and SN 2019ofm. The prominent spectral features of Si II, O I, and Ca II are marked.

mechanism (Piro & Nakar 2014; Sell et al. 2015). These velocity estimates are also necessary for quantitative estimates of the explosion kinetics (Arnett 1982; Arnett et al. 1985). We follow procedures similar to those used in Liu et al. (2016) and Fremling et al. (2018) for normal stripped-envelope SNe. He I is the most common spectral feature near peak light in the sample of Ca-Ib/c events, and hence we estimate the velocity of the He I λ5876 line by fitting a low-order polynomial to the flux around the line. We estimate the uncertainties in the velocity by Monte Carlo sampling of the flux in the relevant wavelength region.

We estimate the flux uncertainty by subtracting the smooth polynomial fit from the spectral data and compute the noise rms as the standard deviation of the flux from the smoothed spectrum. We then add a Gaussian distribution of noise to the spectrum using the wavelength-dependent flux rms as the standard deviation, and compute the spectral fit parameters for the several realizations of the input spectrum. While O I λ7774 is also detected in most of the peak light spectra, we do not fit the absorption in this line since it appears to be uniformly contaminated by another nearby absorption feature (likely Mg II; e.g., Valenti et al. 2014; De et al. 2018a). We perform the same fitting for the He I λ7065 line in the spectra where it is detected in the Ca-Ib/c events, while the same is computed for the Si II λ6355 line in the case of the Ca-Ia events.

The velocity estimates from fitting He I λ5876 and λ7065 are largely consistent in the Ca-Ib/c events. However, the velocities and detection of He in the red events are complicated

Table 4
Spectral Fit Parameters for the Sample of Ca-rich Gap Transients Presented in This Paper, together with the Fits for the Literature Sample of Ca-rich Gap Transients

Object	Phase (days)	V_1 (km s^{-1})	V_2 (km s^{-1})	[Ca II]/[O I]	References
SN 2018ckd	+1	9660 ± 110 (λ5876)	10090 ± 140 (λ7065)	⋯	This work
SN 2018ckd	+10	8260 ± 650 (λ5876)	⋯	⋯	This work
SN 2018ckd	+58	⋯	⋯	>3.38	This work
SN 2018lqo	−2	8230 ± 150 (λ5876)	8270 ± 100 (λ7065)	⋯	This work
SN 2018lqo	+49	5090 ± 310 (λ5876)	⋯	>12.51	This work
SN 2018lqu	+1	11100 ± 410 (λ5876)	10550 ± 280 (λ7065)	⋯	This work
SN 2018lqu	+31	5720 ± 500 (λ5876)	...*	>8.38	This work
SN 2018gwo	+23	5150 ± 570 (λ5876)	⋯	⋯	This work
SN 2018gwo	+53	4780 ± 100 (λ5876)	6660 ± 80 (λ7065)	5.16 ± 0.08	This work
SN 2018gwo	+146	⋯	⋯	3.98 ± 0.06	This work
SN 2018gwo	+243	⋯	⋯	2.70 ± 0.08	This work
SN 2018kjy	+1	...*	2470 ± 170 (λ7065)	⋯	This work
SN 2018kjy	+22	6610 ± 90 (λ5876)	⋯	⋯	This work
SN 2018kjy	+111	⋯	⋯	4.44 ± 0.24	This work
SN 2019hty	+4	7480 ± 120 (λ5876)	8200 ± 50 (λ7065)	⋯	This work
SN 2019hty	+5	8200 ± 1140 (λ5876)	7600 ± 350 (λ7065)	⋯	This work
SN 2019hty	+38	⋯	⋯	>3.27	This work
SN 2019ofm	−2	⋯	7380 ± 230	⋯	This work
SN 2019ofm	+168	⋯	⋯	>2.15	This work
SN 2019pxu	+0	10310 ± 430 (λ5876)	...*	⋯	This work
SN 2019pxu	+8	9320 ± 100 (λ5876)	3110 ± 80 (λ7065)	⋯	This work
SN 2019pxu	+32	7790 ± 90 (λ5876)	3650 ± 180 (λ7065)	⋯	This work
SN 2019pxu	+146	⋯	⋯	>8.30	This work
SN 2005E	−2	10200 ± 200 (λ5876)	9800 ± 80 (λ7065)	⋯	[1]
SN 2005E	−1	10260 ± 60 (λ5876)	9960 ± 60 (λ7065)	⋯	[1]
SN 2005E	+20	4450 ± 230 (λ5876)	4980 ± 60 (λ7065)	⋯	[1]
SN 2005E	+53	4430 ± 80 (λ5876)	4540 ± 150 (λ7065)	8.39 ± 0.26	[1]
SN 2007ke	+20	4370 ± 100 (λ5876)	4210 ± 310 (λ7065)	⋯	[1]
PTF 09dav	+2	⋯	6140 ± 100 (λ6355)	⋯	[2]
PTF 09dav	+8	⋯	5070 ± 70 (λ6355)	⋯	[2]
PTF 09dav	+13	⋯	5070 ± 120 (λ6355)	⋯	[2]
PTF 09dav	+88	⋯	⋯	>22.35	[2]
SN 2010et	+2	8210 ± 70 (λ5876)	8880 ± 60 (λ7065)	⋯	[3]
SN 2010et	+27	7340 ± 110 (λ5876)	7990 ± 120 (λ7065)	⋯	[3]
SN 2010et	+62	3620 ± 440 (λ5876)	7080 ± 360 (λ7065)	⋯	[3]
SN 2010et	+87	⋯	⋯	6.15 ± 0.51	[3]
SN 2010et	+115	⋯	⋯	6.14 ± 1.36	[3]
PTF 11bij	+45	⋯	⋯	>7.06	[3]
SN 2012hn	−3	7230 ± 320 (λ5800)	⋯	⋯	[4]
SN 2012hn	+4	7400 ± 160 (λ5800)	⋯	⋯	[4]
SN 2012hn	+6	7490 ± 70 (λ5800)	⋯	⋯	[4]
SN 2012hn	+13	6740 ± 220 (λ5800)	⋯	⋯	[4]
SN 2012hn	+25	5200 ± 40 (λ5800)	⋯	⋯	[4]
SN 2012hn	+150	⋯	⋯	2.25 ± 0.05	[4]
PTF 11kmb	+1	11670 ± 50 (λ5876)	9910 ± 40 (λ7065)	⋯	[5]
PTF 11kmb	+24	8520 ± 170 (λ5876)	7320 ± 260 (λ7065)	⋯	[5]
PTF 11kmb	+89	⋯	⋯	8.97 ± 0.30	[5]
PTF 11kmb	+124	⋯	⋯	10.07 ± 0.70	[5]
PTF 12bho	+9	7210 ± 170 (λ5876)	3010 ± 50 (λ7065)	⋯	[5]
PTF 12bho	+17	7520 ± 250 (λ5876)	3520 ± 300 (λ7065)	⋯	[5]
PTF 12bho	+51	⋯	⋯	12.10 ± 0.66 (λ5876)	[5]
PTF 12bho	+129	⋯	⋯	>9.57	[5]
SN 2016hgs	−8	15010 ± 200 (λ5876)	11120 ± 310 (λ7065)	⋯	[6]
SN 2016hgs	−4	12880 ± 110 (λ5876)	10610 ± 400 (λ7065)	⋯	[6]
SN 2016hgs	+1	10750 ± 100 (λ5876)	10200 ± 90 (λ7065)	⋯	[6]
SN 2016hgs	+28	⋯	⋯	>4.80	[6]
SN 2016hgs	+59	⋯	⋯	11.52 ± 4.37	[6]
SN 2016hnk	−3	⋯	10350 ± 60 (λ6355)	⋯	[7]
SN 2016hnk	−2	⋯	10020 ± 30 (λ6355)	⋯	[7]
SN 2016hnk	−1	⋯	9740 ± 20 (λ6355)	⋯	[7]
SN 2016hnk	+0	⋯	9690 ± 40 (λ6355)	⋯	[7]
SN 2016hnk	+1	⋯	9610 ± 90 (λ6355)	⋯	[7]
SN 2016hnk	+1	⋯	9720 ± 90 (λ6355)	⋯	[7]

Table 4
(Continued)

Object	Phase (days)	V_1 (km s^{-1})	V_2 (km s^{-1})	[Ca II]/[O I]	References
SN 2016hnk	+1	⋯	9850 ± 130 (λ6355)	⋯	[7]
SN 2016hnk	+3	⋯	9060 ± 70 (λ6355)	⋯	[7]
SN 2016hnk	+4	⋯	8760 ± 50 (λ6355)	⋯	[7]
SN 2016hnk	+6	⋯	8590 ± 40 (λ6355)	⋯	[7]
SN 2016hnk	+6	⋯	8200 ± 160 (λ6355)	⋯	[7]
SN 2016hnk	+8	⋯	8440 ± 760 (λ6355)	⋯	[7]
SN 2016hnk	+10	⋯	7970 ± 110 (λ6355)	⋯	[7]
SN 2016hnk	+16	⋯	6820 ± 70 (λ6355)	⋯	[7]
SN 2016hnk	+26	⋯	6250 ± 140 (λ6355)	⋯	[7]
SN 2016hnk	+31	⋯	5880 ± 80 (λ6355)	⋯	[7]
SN 2016hnk	+32	⋯	5760 ± 210 (λ6355)	⋯	[7]
SN 2016hnk	+35	⋯	5610 ± 90 (λ6355)	⋯	[7]
SN 2016hnk	+47	⋯	5080 ± 110 (λ6355)	⋯	[7]
SN 2016hnk	+265	⋯	⋯	>4.07	[8]

Note. For each spectrum, we measured both the He I λ5876 and λ7065 velocity (if detected) for the Ca-Ib/c events, and only the Si II λ6355 velocity for the Ca-Ia events. We indicate the line measured in brackets next to the velocity measurements for each spectrum phase. Values denoted by * indicate epochs where the S/N of the spectrum was not high enough in the region of interest to measure the specific parameter. The velocity for SN 2012hn was measured using the feature near 5800 Å at peak light since it did not exhibit He signatures. For phases where the spectrum exhibited nebular emission features, we report the measured [Ca II]/[O I] ratio or lower limits when [O I] was not detected (see text). Archival spectra were obtained from the Weizmann Interactive Supernova Data Repository (WISeREP; Yaron & Gal-Yam 2012). The data were originally published in [1] Perets et al. (2010), [2] Sullivan et al. (2011), [3] Kasliwal et al. (2012), [4] Valenti et al. (2014), [5] Lunnan et al. (2017), [6] De et al. (2018a), [7] Galbany et al. (2019), and [8] Jacobson-Galán et al. (2020).

(This table is available in its entirety in machine-readable form.)

by several factors. While SN 2019hty shows an unambiguous presence of both of the He I lines we measure, the λ7065 line absorption in the other objects is contaminated by emission from a nearby blueward feature (see Figure 7), which could be associated with C II (Valenti et al. 2014) or Al II (Kasliwal et al. 2012; De et al. 2018a). Thus, the He I velocities are discrepant between the two lines for these objects. However, we report all these measurements for completeness.

SN 2012hn does not show clear signs of He I in its peak light spectra, and hence we compute the velocity for the nearby 5800 Å feature (suggested to be due to Na I or Cr II in Valenti et al. 2014) assuming that the peak of the feature near maximum light corresponds to the rest wavelength of the line. The low S/N and resolution of the spectrum of SN 2018gwo do not allow us to conclusively identify He I, and hence we do not measure the corresponding velocity for this object. SN 2018kjy exhibits a peculiar peak light spectrum with a large number of low-velocity (∼2500 km s^{-1}) lines. While He I λ7065 is identifiable in the peak light spectrum, we caution that due to the large number of low-velocity lines, we only tentatively identify He I λ5876 in the peak light spectrum.

In Figure 10, we plot the evolution of the prominent photospheric-phase He I λ5876 and λ7065 (for the Ca-Ib/c events) and Si II λ6355 line (for the Ca-Ia events) velocities as a function of phase from the *r*-band peak. For comparison, we also plot the evolution of the He I line velocities observed in the sample of normal SNe Ib presented in Liu et al. (2016). The He I λ7065 velocity in most of the red events is much lower than that in the events with green continua. As stated in Section 3.1.3, this discrepancy is due to the blending of a nearby emission feature blueward of λ7065 that contaminates the velocity measurement, thus making the velocity evolution uncertain. SN 2018kjy stands out as a peculiar low-velocity event as evident from the large number of narrow lines visible in its peak light spectrum (see Figure 5), exhibiting several similarities to the low-velocity spectrum observed in PTF 12bho. SN 2012hn does not exhibit signatures of He I in its peak light spectrum and hence we show the velocity evolution of the nearby 5800 Å feature, likely associated with Na I.

It is worth noting that the Si II λ6355 velocities in the Ca-Ia events vary—both PTF 09dav and SN 2019ofm exhibit lower (by ≈3000 km s^{-1}) velocities than SN 2016hnk at peak (≈11,000 km s^{-1}). The combined sample of photospheric-phase velocities shows a consistent trend of decreasing velocities with time, consistent with a receding photosphere (in mass coordinates) in the SN ejecta. Comparing this to the normal Type Ib events in the comparison sample, we find that while the photospheric velocities are similar near peak light, the Ca-rich gap transients exhibit a much faster drop to low photospheric velocities around ≈20 days after peak light. A faster drop in photospheric-phase velocities suggests that the photospheric line-forming regions recede into the inner and slower layers of the ejecta faster than normal SNe Ib, consistent with the lower ejecta masses and faster transition to the optically thin nebular phase observed in these events.

3.2. Nebular-phase Spectra

3.2.1. The Ca-Ib/c Class

In Figure 11, we show a comparison of the nebular-phase spectra of the Ca-Ib/c class of objects. Despite the diversity in photospheric-phase colors and velocities, the nebular-phase spectra are relatively homogeneous, and are dominated by strong [Ca II] emission and weak [O I] emission (if [O I] is detected at all). The low-velocity events SN 2018kjy and SN 2019pxu exhibit double-peaked lines near the [Ca II] doublet early in the nebular phase, similar to those observed in PTF 12bho (Lunnan et al. 2017), although later spectra exhibit a single unresolved [Ca II] feature. Since SN 2018gwo